

Copyright

by

Timothy Bryce Phillips

2019

**The Dissertation Committee for Timothy Bryce Phillips Certifies that this is the approved version of the following Dissertation:**

**DEVELOPMENT OF A FEEDFORWARD LASER CONTROL  
SYSTEM FOR IMPROVING COMPONENT CONSISTENCY IN  
SELECTIVE LASER SINTERING**

**Committee:**

Joseph J. Beaman, Supervisor

Scott Fish

Thomas Milner

Carolyn Seepersad

Richard Crawford

**DEVELOPMENT OF A FEEDFORWARD LASER CONTROL  
SYSTEM FOR IMPROVING COMPONENT CONSISTENCY IN  
SELECTIVE LASER SINTERING**

**by**

**Timothy Bryce Phillips**

**Dissertation**

Presented to the Faculty of the Graduate School of  
The University of Texas at Austin  
in Partial Fulfillment  
of the Requirements  
for the Degree of

**DOCTOR OF PHILOSOPHY**

**The University of Texas at Austin**

**May 2019**

## **Acknowledgements**

I would like to thank my advisor Dr. Joseph Beaman for accepting me into his research group and opening my eyes to the world of additive manufacturing. He has been an endless source of knowledge and inspiration and I am grateful he allowed me to pursue the research presented here. I would also like to thank Dr. Scott Fish for handling day-to-day operations and helping guide my research. His patience, support, and wisdom have molded me into the researcher I am, and I can only hope some of his project management skills have rubbed off on me.

I would like to thank my lab mates for always being there to bounce ideas off and to lend a hand. It would not be possible for me to have completed this research without them.

I would like to thank my family for their support and encouragement that allowed me to pursue my PhD. They have always been there for me and never hesitate to give me their advice.

Lastly, I would like to acknowledge the instrumental research support of the US Department of Defense (DoD) Air Force Research Laboratory (AFRL) Project # FA8650-17-C-5716 P00003: Laser Additive Manufacturing Pilot Scale (LAMPS) III: Advanced Process Monitoring and Control (PI: Scott Fish).

## **Abstract**

# **DEVELOPMENT OF A FEEDFORWARD LASER CONTROL SYSTEM FOR IMPROVING COMPONENT CONSISTENCY IN SELECTIVE LASER SINTERING**

Timothy Bryce Phillips, Ph.D.

The University of Texas at Austin, 2019

Supervisor: Joseph J. Beaman

Selective Laser Sintering makes up a significant portion of the polymer additive manufacturing market and is often the process of choice for structurally significant polymer components. With its expanding market, especially among end-use components, comes a growing need for improving reproducibility. Components built using Selective Laser Sintering display a large range among their mechanical properties and it has been shown that the thermal history of the building process has a strong influence over these variations. Temperature fluctuations of just a few degrees can mean the difference between scrapped parts or those with excellent mechanical and dimensional properties.

This dissertation will introduce a novel method of reducing temperature and mechanical variations among parts. Physical simulations and empirical measurements of laser-polymer interaction are evaluated and used to guide development of an advanced laser power controller. The feedforward control system developed uses thermal imagery and dynamic surrogate modeling to systematically modulate laser energy impinging on the polymer surface to homogenize post-sintering temperatures. Results from thermal

and mechanical tests will be presented, showing the laser control system is capable of reducing standard deviations by up to 57% for post-sintering temperature and 45% for ultimate flexural strength.

## Table of Contents

List of Tables .....	x
List of Figures .....	xi
Chapter 1: Introduction .....	1
1.1 Selective Laser Sintering .....	1
1.1.1 LAMPS Research Machine .....	2
1.2 Properties of Nylon .....	3
1.3 Infrared Thermography .....	5
1.4 Current Shortcomings .....	8
1.5 Literature Review .....	10
1.5.1 Temperature Sensing .....	11
1.5.2 Process Signature Monitoring .....	14
1.5.3 Additive Manufacturing Application .....	15
Chapter 2: Modeling of SLS .....	18
2.1 Simulation Approach .....	18
2.2 Thermal Model .....	19
2.3 Simulation Results .....	21
Chapter 3: Laser-Polymer Interaction .....	26
3.1 Temperature Measurements .....	26
3.2 Laser Power Modulation .....	31
3.3 Results and Discussion .....	33
Chapter 4: Component-Level Laser Power Control for Simple Geometries .....	38
4.1 Controller Design .....	38

4.1.1 Immutable Empirical Model .....	39
4.1.2 Dynamic Surrogate Model .....	43
4.2 Experiments .....	46
4.2.1 Polymer Structure .....	46
4.2.2 Flexural Strength.....	50
4.3 Results and Discussion .....	53
Chapter 5: Feed-Forward Active Laser Control .....	62
5.1 Position-Based Laser Power Controller Design .....	62
5.2 Controller Design.....	65
5.2.1 Thermal Analysis .....	65
5.2.2 Build Control Model.....	68
5.2.3 Execute Sintering.....	72
5.3 Controller Implementation.....	75
5.4 Experiments .....	77
5.5 Results and Discussion .....	78
Chapter 6: Conclusions .....	81
6.1 Summary of Results.....	81
6.2 Broader Impact .....	82
6.3 Future Work.....	83
Appendices.....	86
Appendix A: List of Terms and Abbreviations .....	86
Appendix B: Selected Code.....	88
Perspective Transformation .....	88

Add Thermal Measurements to Model .....	89
Power Surface Regression .....	90
Apply Binary Mask.....	91
Point In Polygon Test .....	91
Works Cited .....	92

## **List of Tables**

Table 1.1 Properties of Nylon 12 produced by Advanced Laser Materials.....	3
Table 2.1 Boundary and initial conditions for thermal model.....	19
Table 2.2 Standard parameters for nylon SLS used in finite volume analysis .....	21
Table 3.1 Results of vector-level power control.....	36

## List of Figures

Figure 1.1: Differential scanning calorimetry curve for ALM PA650 nylon 12 [11] .....	4
Figure 1.2: Blackbody spectral emittance (a) over the electromagnetic spectrum for 500 K to 900 K and (b) in the mid-wave infrared spectrum for 440 K to 470 K.....	6
Figure 1.3: Correlation between processing temperature and tensile strength .....	9
Figure 2.1 Thermal model control volume .....	20
Figure 2.2 Initial conditions of thermal simulation showing a side view of (a) starting temperature and (b) starting melt fraction .....	23
Figure 2.3 Melt fraction when applying a constant laser power to powder with non- constant temperature .....	24
Figure 2.4 Melt fraction when applying a variable laser power to powder with non- constant temperature .....	25
Figure 3.1 Thermal measurement from FLIR SC8240 camera .....	27
Figure 3.2 Pre- and Post-sintering temperature comparison with 10% laser power.....	28
Figure 3.3 Pre- and Post-sintering temperature comparison with 45% laser power.....	28
Figure 3.4 Pre- and Post-sintering temperature comparison with stepped laser power.....	29
Figure 3.5 Multiple vectors showing laser power and temperature increase.....	30
Figure 3.6 Single vector transfer function for laser power to temperature increase.....	31
Figure 3.7 Simulated results from dynamic sectioning algorithm.....	33
Figure 3.8 Pre-sintering temperature profile for in-situ vector power control .....	34
Figure 3.9 Optimal laser power of dynamically sectioned vector. ....	34
Figure 3.10 In-situ vector-level control results.....	36
Figure 4.1 Temperature increase vs laser power transfer function for various positions in the powder bed.....	40

Figure 4.2 Baseline results for non-controlled laser sintering showing (a) a composite max post-sintering image and (b) the temperature profile along the vector indicated .....	42
Figure 4.3 Results from using the immutable empirical model showing (a) the presintering temperature and calculated laser power profile and (b) the resulting post-sintering temperature profile .....	43
Figure 4.4 Dynamic surrogate model-based laser power controller block diagram .....	44
Figure 4.5 Example of a dynamic laser power model .....	46
Figure 4.6 Example DSC results of PET demonstrating how to calculate enthalpy [68]..	47
Figure 4.7 DSC results for nylon 12 showing the double melting peaks [71].....	49
Figure 4.8 Nylon 12 samples prepped for DSC .....	50
Figure 4.9 Flexure specimens build location and control pattern on (a) odd numbered builds and (b) even numbered builds .....	51
Figure 4.10 Flexure specimen delaminating under load.....	53
Figure 4.11 Temperature distribution for DSC samples.....	54
Figure 4.12 Temperature results from flexure specimens .....	55
Figure 4.13 Laser power results from flexure specimens .....	56
Figure 4.14 DSC curve for nylon 12 sample .....	57
Figure 4.15 Correlation of enthalpy with sample mass .....	57
Figure 4.16 Microscopy images of sintered nylon 12 samples taken during DSC at approximately (a) 170 °C, (b) 178 °C, (c) 185 °C, and (d) 200 °C .....	58
Figure 4.17: Flexural strengths of both control styles shown as (a) a histogram and (b) a Gaussian distribution plotted against their respective means .....	60
Figure 4.18 Ultimate flexural strength vs average post-sintering temperature.....	60
Figure 5.1 Position-Based Laser Power Controller .....	64

Figure 5.2 Thermal image registration process showing the laser sintered geometries on the left, (a) the raw thermal image, and (b) the registered image on the right with the laser sintered geometry overlaid.....	66
Figure 5.3 Laser scan files with their associated binary masks showing sintering patterns.....	68
Figure 5.4 Images depicting (a) a composite max image after coordinate transformation into machine space, (b) the binary mask created from scan file, and (c) the composite max image with binary mask applied. ....	69
Figure 5.5 Example dataset after (a) 3 layers and (b) 4 layers showing the change in linear regression coefficients and how the weighting decreases due to the forgetting factor .....	71
Figure 5.6 Example laser power model at position $x = 0$ , $y = 10$ after 10 layers of data ..	71
Figure 5.7 Thermal data showing (a) a registered pre-sintering image, (b) the desired temperature increase assuming a desired post-sintering temperature of 195 °C, and (c) the binary sintering mask for the upcoming layer applied to the desired temperature increase image. ....	73
Figure 5.8 Example of power surface weighting for a component with non-constant geometry showing (a) a component with an unsupported overhang and a top down view of layers (b) 80 and (c) 81, where the step geometry change occurs. The orange grids show the 1mm x 1mm areas used in the thermal models with the number of data points for each grid overlaid. ....	74
Figure 5.9 Example power surface sent to PBLP controller.....	75
Figure 5.10 Dimensions of (a) test component and (b) their arrangement within the build chamber.....	77

Figure 5.11 Results of baseline temperature testing of a complex geometry .....	79
Figure 5.12 Results of Automated Laser Control temperature testing of a complex geometry .....	80
Figure 5.13 Improvement in temperature uniformity when using Automated Laser Control for a complex geometry .....	80

## **Chapter 1: Introduction**

### **1.1 SELECTIVE LASER SINTERING**

Selective Laser Sintering (SLS) is a powder bed fusion (PBF) additive manufacturing (AM) process that was developed at the University of Texas at Austin in the 1980's [1] [2]. It uses a high-powered laser to create complex 3D components out of polymer powders directly from computer-aided design (CAD) geometry [3]. SLS is unique among other additive manufacturing processes in that it can produce components without the need for support structures. This allows for faster production, 3D stacking of components inside the build environment, and less post-processing. SLS is one of the most common industrial AM techniques for producing functional plastic components [4].

To create a part in an SLS machine, a designer first uses CAD software to produce a 3D model. A slicing program is used to turn the 3D model into a stack of 2D geometries, each one approximately 100 $\mu$ m thick. Each 2D geometry is then reduced to a series of vectors and contours that describe the laser scan path that will be used to create that cross-section. Inside the SLS machine, a thin layer of powdered polymer is spread and allowed to come to the working temperature. The laser scanning system uses galvanometers to direct laser energy onto the powder in a pattern determined by the 2D geometry. Once this layer of powder has been fused together, the recoat mechanism spreads a new layer of powder and the process repeats with the subsequent 2D geometry. The laser scanning system not only fuses each layer to itself, but also to the layers below it, producing fully 3D components.

### **1.1.1 LAMPS Research Machine**

All SLS testing and control implementation discussed in this dissertation was accomplished on the research machine at the University of Texas at Austin known as the Laser Additive Manufacturing Pilot System (LAMPS). This section will briefly cover some of the pertinent features of LAMPS, but more information on its development can be found in Fish et al. [5]. LAMPS was designed with an open architecture for process control research and has a heated build environment capable of maintaining temperatures up to 400°C. To accomplish this, all bearings, electronics, and heat sensitive components are housed externally of the build chamber. The machine contains over 40 strip heaters, each with their own thermocouple and Proportional-Integral-Derivative (PID) controller, allowing fine adjustment and control over the environmental temperature. LAMPS also contains 3 Heraeus Unum 1,320 watt quartz lamp infrared (IR) heaters. These quartz lamps have a directional energy output and a fast response time. They are controlled in a feedback loop using data from one of LAMPS' IR cameras, with two of the quartz lamps being used to control the build surface temperature and the third used to flash pre-heat the powder dropped into the chamber prior to spreading, for each layer.

In addition to the thermocouple feedback, LAMPS utilizes multiple IR cameras to measure powder temperature. A FLIR A6701sc Mid-Wave Infrared (MWIR) camera is used as the quartz lamp feedback source. This MWIR camera is capable of recording 640x512 pixel images at 60 Hz. This camera is used heavily for the control techniques discussed in this dissertation and more information on its function can be found in section 1.3. LAMPS also has the capability of using an Optical Coherence Tomography (OCT) sensor to provide valuable information about the powder surface and melt quality. Additional information on OCT and its utility in SLS can be found in Lewis et al [6] and Gardner et al [7].

## 1.2 PROPERTIES OF NYLON

The experiments discussed in this dissertation were all performed in Advanced Laser Materials' (ALM) PA650 nylon 12, a common AM polymer. While the control techniques discussed here are not limited to nylon and are applicable to any SLS material, nylon is one of the most common SLS materials and thus provided a well-understood platform for testing. Nylon 12, also known as polyamide 12 or polylauro lactam, has been estimated to make up 90-95% of SLS materials [8] [9]. It is used so extensively in SLS due to its superior mechanical properties and chemical resistance as well as its favorable thermal properties. Some of the pertinent properties of ALM PA650 are shown in table 1.1 [10].

<b>Bulk Density</b>	0.46 g/cc	<b>Average Particle Size</b>	55 $\mu\text{m}$
<b>Sintered Part Density</b>	1.02 g/cc	<b>Particle Size Range</b>	30-100 $\mu\text{m}$
<b>Melting Point</b>	181 $^{\circ}\text{C}$	<b>Ultimate Tensile Strength</b>	48 MPa

Table 1.1 Properties of Nylon 12 produced by Advanced Laser Materials

Nylon 12 is a semi-crystalline polymer, meaning it has a highly ordered molecular structure with a defined melting temperature. As such, the term Selective Laser Sintering is a misnomer as the primary consolidation method during SLS of nylon is melting rather than sintering. Other researchers have used differential scanning calorimetry (DSC) to measure the melting temperature of nylon 12 and have found the true melting peak to be closer to 187  $^{\circ}\text{C}$ , though the melting onset does begin around 181  $^{\circ}\text{C}$ , in agreement with the specifications provided by ALM [8] [11]. One of those DSC curves is reproduced in figure 1.1 [11]. The DSC curve also shows recrystallization onset around 148  $^{\circ}\text{C}$ . When cooling a (semi)crystalline polymer, this temperature generally identifies the point at

which the polymer crystals nucleate and begin to grow, though there is evidence that recrystallization occurs in SLS at temperatures as high as 168 °C [12].

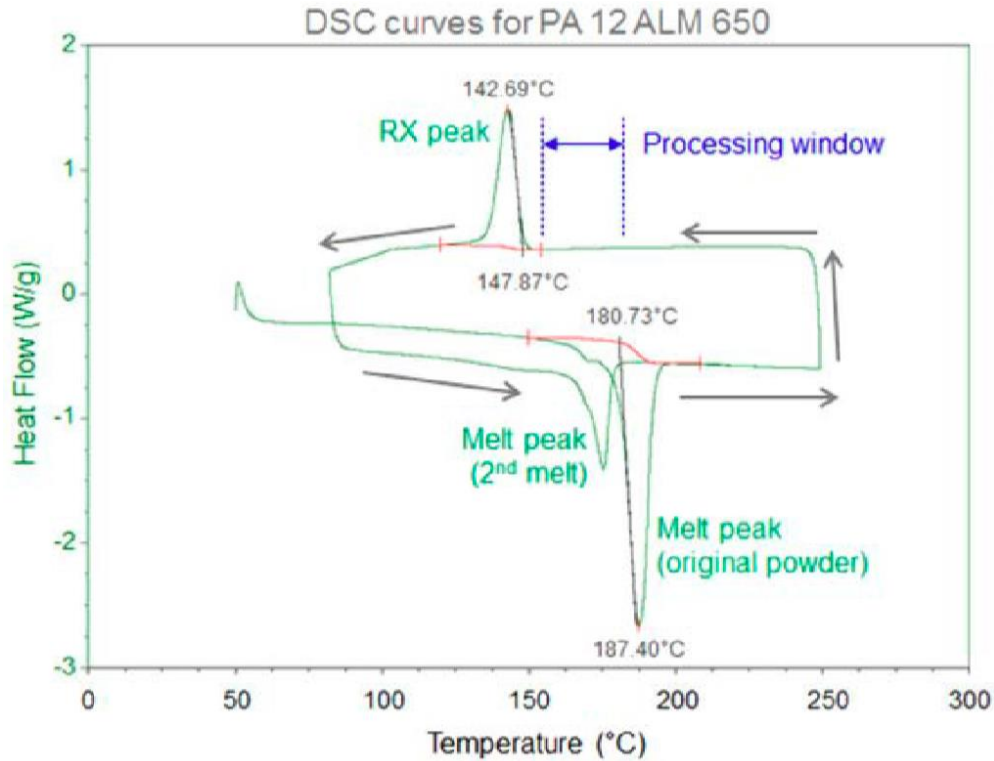


Figure 1.1: Differential scanning calorimetry curve for ALM PA650 nylon 12 [11]

The range between melt temperature and recrystallization temperature is referred to as the processing window. The polymer must be preheated within this range in order to be used in the SLS process. The traditional understanding of SLS polymer consolidation is that by preheating the powder within the processing window and selectively melting sections with a laser, both molten and crystalized states can coexist at the same temperature. Once the entire component is built, its temperature is gradually reduced and the component is allowed to recrystallize. In doing so, dimensional inaccuracies such as curl are kept to a minimum. The challenge here is that DSC tests are performed under controlled conditions that are not present during the SLS process. The

heating and cooling rates can affect the melting and recrystallization temperatures and the real-life processing window is much smaller than indicated via DSC. Thus, the target preheat temperature for polymers is typically just a few degrees below the melting temperature [8].

### **1.3 INFRARED THERMOGRAPHY**

In order to use any non-contact thermal measurement sensors (pyrometers, infrared cameras, etc.) it is essential to understand infrared thermography and how it applies to temperature measurements. Infrared thermography relies on the fact that all objects emit radiation, the amount of which can be related to that object's temperature through the Stefan-Boltzmann law [13]. Planck's law for blackbody radiation, found in equation 1.1, describes the spectral density of radiation emitted by an object based on its temperature [14]. By measuring the spectral output of an object at a known wavelength or range of wavelengths, that object's temperature can be calculated. The radiation emission curves for different temperatures can be seen in figure 1.2. The infrared spectrum is typically split into three regions: short-wave infrared (SWIR) between 1.2-2.4  $\mu\text{m}$ , mid-wave infrared (MWIR) between 3-5  $\mu\text{m}$ , and long-wave infrared (LWIR) 8-13  $\mu\text{m}$  [13].

As an object heats up, its photonic emission increases in magnitude and decreases in wavelength. As such, SWIR is typically used for measuring high temperature objects with temperatures in excess of 1,000 C. The radiation at most polymer melting points is comparatively small in this spectrum, making SWIR thermography not practical in polymer SLS. The spectral emittance in MWIR and LWIR bands at nylon melting temperature is on the same order of magnitude, making both appropriate for SLS sensors.

There are other considerations, though, that elevate the utility of MWIR over LWIR for polymer SLS. The majority of polymer SLS machines use a CO<sub>2</sub> laser with a central wavelength of 10.6 μm [15]. This places the radiation emitted by the laser within the LWIR band, meaning an LWIR sensor will detect reflected laser radiation. This will negatively impact the temperature reading in an LWIR sensor and has the potential to damage it if the radiation is intense enough. This makes MWIR sensors the best choice for measurement of laser interaction in polymer SLS.

$$M_b(\lambda, T) = \frac{2\pi hc^2}{\lambda^5 [\exp(\frac{hc}{\lambda kT}) - 1]}, \frac{W}{m^2 \mu m} \quad \text{EQ 1.1}$$

$M_b$  = Spectral Emittance  
 $T$  = Temperature

$h$  = Planck's Constant  
 $\lambda$  = Wavelength

$k$  = Boltzmann's Constant  
 $c$  = Speed of Light

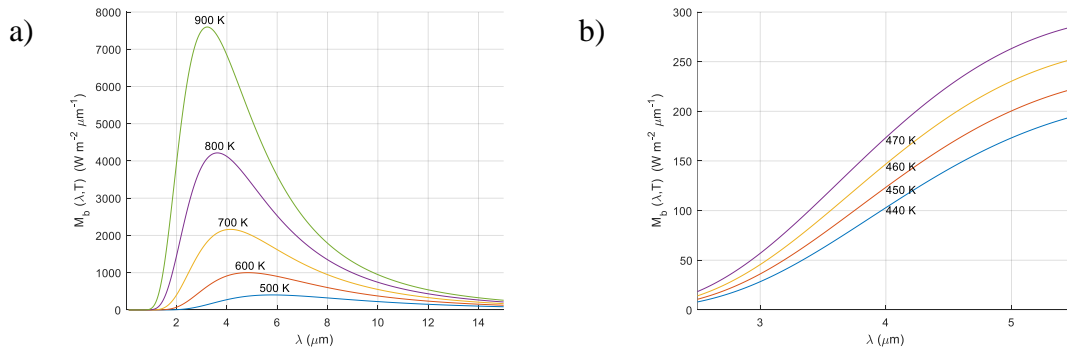


Figure 1.2: Blackbody spectral emittance (a) over the electromagnetic spectrum for 500 K to 900 K and (b) in the mid-wave infrared spectrum for 440 K to 470 K

Planck's Law given in equation 1.1 is an idealization of the spectral output based on the assumption that the object is a perfect blackbody. In real materials, only a fraction of this blackbody radiation is emitted. The ratio of actual emittance to the blackbody emittance for an object of the same temperature is known as emissivity, as seen in

equation 1.2. Nylon, in its powdered form used in SLS, has an emissivity of approximately 0.95 [16].

$$\epsilon = \frac{M(T)}{M_b(T)} \quad \text{EQ 1.2}$$

$\epsilon = \text{Emissivity}$        $M = \text{Actual emittance}$        $M_b = \text{Blackbody emittance}$

In order to obtain an accurate temperature reading using infrared thermography, not only does the emissivity of the object need to be known, but also information about the environment the object is in. As stated earlier, all objects emit radiation and everything within the scene can affect the amount of radiation that impinges on the thermography sensor. In the case of an additive manufacturing system, there are many external factors that need to be accounted for. Simplified equations for incorporating some external radiation sources and isolating the target temperature are seen in equations 1.3 and 1.4. In an SLS machine with a heated build chamber, the enclosure emits radiation that can reflect off the target object and affect the measurement by the IR camera, leading to the  $T_{ref}$  correction term in equation 1.4. The build atmosphere also affects the IR camera measurement by reducing all radiation passing through it by its transmission value  $\tau$  and emitting its own radiation, leading to the  $T_{atm}$  correction factor. A complete radiation model of the SLS system would also include the contribution by the zinc-selenide (ZnSe) window that is between the IR camera and the object. Much like the atmosphere, the ZnSe window will affect all radiation passing through it due to its non-perfect transmission and will contribute its own radiation due to being at an elevated temperature.

$$W = \epsilon\tau W_{obj} + (1 - \epsilon)\tau W_{ref} + (1 - \tau)W_{atm} \quad \text{EQ 1.3}$$

$$T_{obj} = \sqrt[4]{\frac{W - (1 - \epsilon)\tau\sigma T_{ref}^4 - (1 - \tau)\sigma T_{atm}^4}{\epsilon\sigma\tau}} \quad \text{EQ 1.4}$$

$W$ = Total Power	$\sigma$ = Stefan-Boltzmann constant	$\epsilon$ = emissivity
$T_{ref}$ = Reflected Radiation Temperature	$T_{atm}$ = Atmospheric Temperature	$\tau$ = Atmospheric Transmission
$W_{obj}$ = Power emitted by target	$W_{ref}$ = Power emitted by environment	$W_{atm}$ = Power emitted by atmosphere

Properly modeling all the radiation sources in an SLS machine that impact the ability to measure the temperature of a target object is rather difficult, as all the correction factors seen in equation 1.4 must be known precisely. Additionally, the transmission of the ZnSe window may not be constant throughout a build [11] and may be non-uniform [17] as contaminants build up on the window during the build process. As a result, it is preferred to adjust these values empirically rather than build a complete model. To do so, a blackbody source at a known temperature is placed within view of the IR camera and the correction factors are iterated in order to make the IR camera reading match the true temperature of the blackbody. Repeating this process over the range of temperatures that are expected during the build process will calibrate the IR sensor over that range.

#### 1.4 CURRENT SHORTCOMINGS

One of the biggest problems with SLS, and AM in general, is that there is a large variation of mechanical properties in parts that it produces. A large body of research suggests that much of this variation comes from the thermal history of the parts during the build process [18] [19] [20] [21] [22] [23]. If too little energy is deposited, the

powder does not fully melt and produces a weak, porous part. If too much energy is deposited, the polymer can decompose, producing a weak part. Also, if the temperature gradient across a part is too large, varying rates of expansion and contraction will cause the part to curl, decreasing its geometrical accuracy [24] [25]. One approach to solving this issue is to improve the bulk powder surface heater system. This approach has shown improvements in thermal control and component quality, but is limited due to the response and relative coarseness of the heater system. More advanced SLS machines use an array of high-energy quartz lamp radiative emitters [26] that are capable of quickly and accurately changing the powder surface temperature, but temperature uniformity across the powder surface is still limited by the number and configuration of the lamps. Even the relatively small temperature differences produced by these more advanced systems can have a large influence on mechanical strength, as seen in figure 1.3.

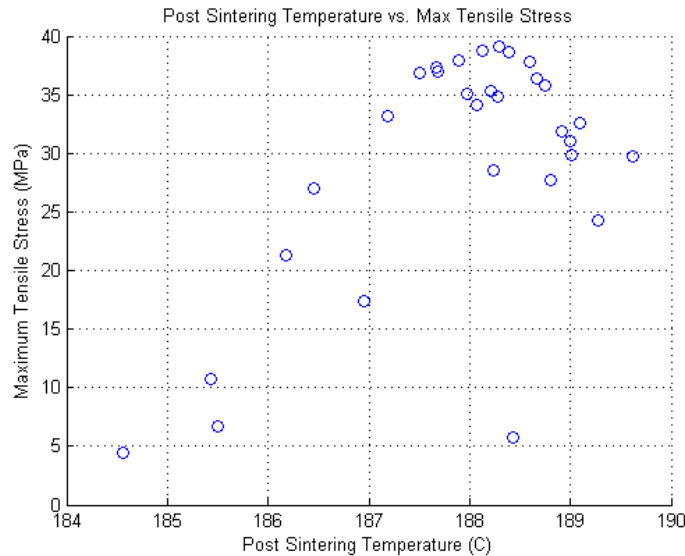


Figure 1.3: Correlation between processing temperature and tensile strength

This dissertation will cover a complimentary approach to improving component uniformity by controlling laser fluence to provide precise heating to the powder bed. The laser can be used as a highly directional heating source and its energy modulated to achieve the desired temperatures in the powder. While research has been done in the past to develop real-time laser monitoring and control systems for metals AM, these techniques are not appropriate for polymer AM. More information on these other systems can be found in the literature review provided in section 1.5. At the melting temperature of steel, the radiant energy emitted is two orders of magnitude larger than that emitted at the melting temperature of nylon. A real-time measurement of polymer melting, then, would require a sensor with significantly increased sensitivity and decreased noise floor. It has also been suggested that the real-time measurement would require 10-20 kHz feedback from the thermal sensor [27]. At the time of writing, an appropriate sensor that meets these requirements is not available for polymer AM real-time control. An alternative approach, proposed in this dissertation, is to use a feedforward control technique. Such a system provides the desired level of control over powder bed temperature yet uses less expensive and readily available hardware.

## **1.5 LITERATURE REVIEW**

Laser sensing and control has been explored previously for processes such as laser welding and laser machining. This section will review some of the techniques used in those processes as well as techniques that have been implemented in AM machines. A comprehensive literature review is presented, though some of the techniques discussed below are not currently applicable to AM.

Sensors used for laser monitoring can be split into two categories: sensing of process temperature, and sensing of process signatures [28]. The first category consists of directly measuring powder temperature while the second consists of measurements such as acoustic signatures, electromagnetic signatures, and melt pool dimensions.

### **1.5.1 Temperature Sensing**

Controlling laser energy deposition based on direct temperature sensing is the most dependable way of controlling powder temperature, but it requires a reliable way of non-contact temperature measurement. The traditional method of non-contact temperature measurement is with the use of pyrometers. By measuring the radiation emitted from an object, a pyrometer can estimate the object's temperature based on equation 1.1. The issue with using this type of temperature measurement is that it is dependent on emissivity,  $\epsilon$ , which for most real-world materials varies with temperature, wavelength, and viewing angle [29]. Pyrometry has been used successfully to monitor laser machining processes [30] but it requires extensive material testing to determine monochromatic emissivities and spectral transparency windows. This type of sensor has seen application in laser machining [31] as well as SLS and SLM, but material characterization and emissivity sensitivity may limit the utility of single wavelength pyrometry for laser control of polymer AM.

While traditional pyrometry requires knowledge of the emissivity, it was discovered that using two pyrometers to measure photons in different spectral bands can produce a measurement that is emissivity-independent. By taking the ratio of the pyrometer signals, the actual temperature can be found using equation 1.5 [32].

$$T_R = \left( \frac{1}{T} + \frac{\ln\left(\frac{\epsilon_1}{\epsilon_2}\right)}{C_2(\lambda_2^{-1} - \lambda_1^{-1})} \right)^{-1} \quad \text{EQ 1.5}$$

$T$  = True temperature

$T_R$  = Measured ratio temperature

$\epsilon_i$  = Emissivity of object in spectral band of pyrometer i

$\lambda_i$  = Wavelength of pyrometer i

$C_2 = \frac{hc}{k}$ , Planck's second radiation constant

The temperature measurement is now dependent on the ratio of the materials' emissivities at the two wavelengths measured, rather than the individual emissivities. The advantage of this approach comes when the material can be considered a gray-body, or its emissivity is wavelength independent. This allows the emissivity ratio to be unity and the absolute temperature to be calculated without knowing the emissivity of the material. However, it is likely that the material being measured does not act exactly as a gray-body, thus careful selection of the pyrometer spectral bands is imperative for minimizing measurement error. There are two factors in the measurement error calculation: the relative wavelengths of the two spectral bands, and the true emissivity in those bands. The likelihood of a material behaving as a gray-body in the two spectral bands selected is higher if the spectral bands are close to one another. However, the closer wavelengths have the opposite effect of increasing the measurement error if there is an emissivity mismatch. The common approach, then, is to select adjacent spectral bands and leverage the fact that there will typically be a smaller discrepancy in material emissivity in the two bands [33].

Another consideration when selecting pyrometer wavelengths is the desired temperature range of the sensor. According to Planck's law, the peak wavelength of radiation emitted from an object depends on the temperature of the object. In order to

build a sensor with a high signal-to-noise ratio, the pyrometer should be sensitive to wavelengths in a spectral band where the object emits enough photons to get a good signal. Much of the research done on two-color pyrometry focuses around measuring elevated temperatures ( $>600$  °C). There are some researchers who have successfully measured temperatures as low as 200 °C by using larger wavebands to capture more radiation [33] [34] and some companies claim to have devices that are sensitive down to 300 °C [35]. This type of sensor has already shown promise in SLM laser sensing applications [36] [37].

Another way of measuring process temperature is through thermal imaging. This works on principles similar to pyrometry and is typically accomplished using an infrared camera but can also be done via CCD or CMOS cameras. IR cameras can use sensors that require active cooling, such as a quantum well infrared photodetector, or uncooled sensors, such as those based on pyroelectrics or microbolometers. While these sensors can be excellent for measuring temperatures spatially, they suffer many of the same drawbacks as single-color pyrometers. They are also typically expensive and lack the frame rate required for real-time control. There are exceptions to this generality, such as a FLIR SC8240, which is capable of recording at 2,243 frames per second but is expensive, or the FLIR Lepton, which costs less than \$200 but can only record at 9 frames per second. These sensors have been used in polymer laser welding control [38] as well as monitoring and control of polymer SLS [39].

In an effort to develop fast, inexpensive thermal imaging devices, some researchers have turned to traditional CCD and CMOS cameras. These sensors are typically found in everyday cameras but can be sensitive up to 900 or 1100 nm [40] [41] [42]. Temperature measurements may be taken using the short-wave infrared (SWIR) region of these cameras. Zauner et al. were able to measure temperatures as low as 350 C

using a CCD camera with a filter wheel controlled via a stepper motor [41]. The spectral edge filters allow for “multi-spectral” imaging of an object. By taking 20-30 frames and stacking the images and employing a Gaussian image pyramid algorithm, noise can be reduced and temperature accuracy is improved. The downside to this technique is the multiple frames required and the computationally expensive image processing, making it more suited to static temperatures rather than measuring a dynamic process.

Expanding on this work, Fu et al. proposed using a multi-peak interference filter to simultaneously obtain multicolor signals [40]. By filtering the light into two spectral bands, Fu was able to take advantage of the emissivity independence property of two-color pyrometry. This system had less than 1.5% error for temperatures greater than 1,000 C.

### **1.5.2 Process Signature Monitoring**

While temperature monitoring is popular and is an effective measure of process quality, it is not the only type of sensing that has application in laser control. It is possible to monitor melt characteristics such as melt pool size, acoustic signature, or plasma plume properties to determine build process quality.

The easiest process signature to measure is the physical size of the melt pool. This monitoring technique has been employed in metal AM using both CMOS cameras and pyrometers [27] [43] [44]. Clijsters et al. propose that real-time monitoring of SLM requires 10-20 kHz sample rate; they were able to record up to 10 MHz, well exceeding what is necessary for real-time monitoring and control. The melt pool created by the laser gives some vital information about the quality of the sintering process. By comparing the current melt pool size and length-to-width ratio with those of a known “good” melt pool, the process can potentially be controlled in real-time. It is also

possible to use a second laser at a different wavelength and lower power to illuminate the melt pool and allow for faster image recording [44]. In polymer SLS, however, the re-solidification rate is so much slower that entire vectors and areas can remain molten, meaning measurements of the melt pool size and length-to-width ratio are not applicable.

Acoustic monitoring is commonly used in laser welding, but at the time of writing there have not been any studies published that apply this approach to additive manufacturing [28]. In laser welding, this approach is used due to the simplicity and low cost of acoustic sensors, and the frequency response of the welding process has been correlated to many weld quality metrics. It has been postulated that the complex build environments of AM would make implementation of acoustic monitoring difficult.

Laser welding and laser melting processes produce a plasma plume above the molten metal that can give some valuable information on the process quality. Chmelockova et al. used a fast spectrometer to measure the optical emission of the plasma created during laser welding and found that the electron temperature of the plasma was dependent on the penetration depth of the weld [45]. This information may be useful as the control input for a real-time control system, but the researchers were unable to implement such a system due to their inability to precisely maintain the position of their optics. Another implementation of plasma monitoring involved placing a photodiode on the opposite side of the material as the laser as a butt weld was formed [46]. This requires positioning the sensor in a position that is not possible with the SLS process.

### **1.5.3 Additive Manufacturing Application**

While there has not been nearly as much work on laser control in AM as there has been with other laser processing techniques, some researchers have begun investigating

it. Kruth et al. have developed a laser interaction monitoring technique for metal AM that uses a pyrometer and a CMOS camera filtered to only accept light in the SWIR region [43]. The camera data is analyzed to examine the melt pool area, width, and length, and the pyrometer provides values for the melt pool intensity. These values are compared with reference data from the same geometrical coordinate in the build chamber. The reference data is compiled in a dot matrix where optimal sensors signals are defined for each type of sintered line (fill lines, outline scans, overlapping lines, overhangs, etc.) at each geometrical coordinate. This is not a trivial task and would require new reference data sets for each minute change in the machine parameters, such as scan speed, material used, vacuum or inert gas flow rate, etc. Researchers at Vulcan Labs have successfully implemented a real-time laser controller using pyrometer feedback in a metals AM machine. They had success in homogenizing the measured radiation emission and, presumably, the temperature [47].

Engineers at Electro Optical Systems (EOS) have developed a feature they refer to as EOSAME that claims to provide temperature-based laser control functionality to their polymer AM machine. The documentation on this feature is limited, with the extent of its function described in a single sentence on their website [48].

The new EOSAME feature adjusts the energy input and thus ensures a homogeneous quality and enhanced mechanical properties of the manufactured parts over the entire building volume.

EOS' relevant patent [49] and description of EOSAME from their engineers [50] [51] paints a more complete picture of how the system works. EOS temporarily installs an IR camera on their SLS machines and uses it to characterize the pre-sintering temperature distribution on the powder surface. This IR camera is then removed and the temperature distribution is assumed to be stable during future builds. This enables them

to use a pyrometer during runtime to measure temperature in a single location and generalize that to infer temperatures across the powder bed. This knowledge combined with material calibration allows them to apply a pre-computed laser power map to homogenize post-sintering temperatures. EOS has had great success with this feature, though it is limited in applicable materials and is dependent on the stability of the machine's temperature distribution. The lack of spatial temperature information places a heavy dependence on machine calibration with little feedback as to its accuracy.

Researchers at the University of Louisville have also created a feedforward control technique for polymer SLS [52] [53]. They found that post-sintering temperatures were dependent on the cross-sectional areas of sintered parts, both of the current layer and previous layers. They used information about past and future layer geometries as inputs to their control model that adjusted laser power in order to attempt to homogenize post-sintering temperatures. The researchers had good success at homogenizing temperatures, though their testing took more of an iterative learning approach where they repeatedly built the same geometry until satisfactory temperature homogenization was achieved after multiple testing iterations. They also did not address position-dependent temperature and laser power transmission fluctuations.

## **Chapter 2: Modeling of SLS**

### **2.1 SIMULATION APPROACH**

This dissertation will focus on implementation of automated laser control techniques based on dynamic surrogate models presented in chapters 3-5. However, a physics-based thermal model is also important for understanding the underlying phenomenon and directing the research. As such, this chapter will review some existing thermal models of the SLS process found in literature. These well-documented models were compiled into a C++ implementation that uses a numerical solution method to calculate temperature and melt percent of polymer within the control volume. This implementation is used to simulate powder reaction to unique situations with respect to polymer temperature and laser power in order to verify some assumptions about the SLS process.

The thermal model described in this chapter is used to answer the questions of (1) what happens when a constant laser power is applied to a powder bed with a temperature gradient, and (2) can modulating the laser power correct for that temperature gradient. This thermal model is not appropriate for real-time model-based control due to its slow solution speed; however, the results from simulations using this thermal model are useful for developing the controllers described in subsequent chapters. Since this thermal model is not novel and is not intended to be implemented in a controller, it was not subjected to a rigorous validation process as part of this dissertation. Proofs for the model can be found in the supporting literature cited below and the simulation results presented in this chapter are to be treated as approximate solutions.

## 2.2 THERMAL MODEL

Heat transfer within the powder bed is governed by the conduction equation found in equation 2.1. Profilometer measurements of the laser reveal it has a Gaussian distribution with half-width half-max radius  $w$ . The laser heating component of the heat transfer equation is found in equation 2.2 [39] [54] [55] [56] [57] [58] [59] [60] [61].

$$\rho c_p \frac{\delta T}{\delta t} = k_t \left( \frac{\delta^2 T}{\delta x^2} + \frac{\delta^2 T}{\delta y^2} + \frac{\delta^2 T}{\delta z^2} \right) + Q(x, y, z, t) \quad \text{EQ 2.1}$$

$\rho$  = Powder density       $c_p$  = Powder specific heat       $k_t$  = Powder thermal conductivity  
 $x, y, z$  = Coordinates within powder bed       $Q$  = Laser source contribution

$$Q(x, y, z, t) = (1 - R)\beta I_o \exp\left(-\frac{(x - v_x t)^2 + (y - v_y t)^2}{w^2} - \beta z\right) \quad \text{EQ 2.2}$$

$Q$  = Gaussian heating       $R$  = Powder reflectivity       $\beta$  = Extinction coefficient  
 $w$  = Radius of Gaussian beam       $x, y, z$  = Coordinates within powder bed       $v_x, v_y$  = Velocity of Gaussian beam

The boundary conditions imposed on the model assume the powder bed is well insulated and that there is a plane of symmetry through the center of the laser beam that runs parallel to its movement. This is seen visually in figure 2.1 and summed up in table 2.1.

<b>Top</b>	$-k_t \frac{\delta T}{\delta z} \Big _{z=0} = h_t(T_a - T_{z=0}) + \epsilon\sigma(T_e^4 - T_{z=0}^4)$
<b>Sides</b>	$-k_t \frac{\delta T}{\delta z} \Big _{x=0, x_{MAX}   y=y_{MAX}   z=z_{MAX}} = 0$
<b>Symmetry Plane</b>	$-k_t \frac{\delta T}{\delta z} \Big _{y=0} = 0$
<b>Initial Conditions</b>	$T(x, y, z, 0) = T_{initial}(x, y, z)$

Table 2.1 Boundary and initial conditions for thermal model

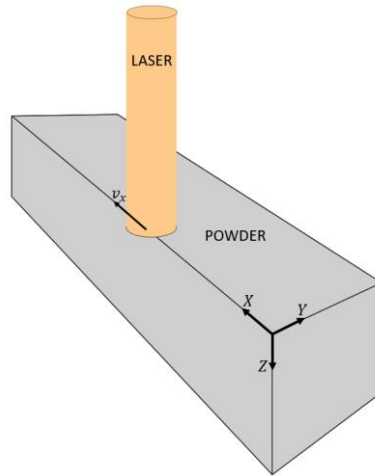


Figure 2.1 Thermal model control volume

A finite volume solution approach was taken by discretizing the powder into voxels. The finite volume method is widely used for evaluating complex models [39] [56] [58] [59] [60] [62]. It allows for numerically solving partial differential equations by evaluating heat flux and temperature changes within each element of the discretized model. It calculates changes in each voxel after infinitesimal changes in time, giving an approximate solution to the model at each time step. Each voxel in the control volume has a temperature and melt percent associated with it. The temperature of each is tracked throughout the solution, with special considerations once the temperature is between the material's solidus and liquidus temperatures. Between these two temperatures, the voxel is undergoing phase change, the amount of which is calculated by comparing the energy entering the voxel with its enthalpy.

In order to obtain high resolution information pertaining to the melt depth of the powder, small voxels were used in the limit that the stability conditions were satisfied and the solution time was reasonable. The discretization stability conditions imposed are  $\min(\Delta x, \Delta y, \Delta z)^2 \geq 2k\Delta t$  and a maximum voxel aspect ratio of 10.

## 2.3 SIMULATION RESULTS

The thermal model and numerical solution method described in this chapter were used to evaluate multiple situations relevant to laser control technique described in this dissertation. Standard parameters for nylon and the laser system used in the LAMPS SLS machine are given in table 2.2.

$w = 340 \mu m$	Laser radius at $\frac{1}{e^2}$ intensity	$\rho_{pow} = 460 \frac{kg}{m^3}$	Powder nylon density
$v = 1.5 \frac{m}{s}$	Laser scan velocity	$\rho_{liq} = 1020 \frac{kg}{m^3}$	Liquid nylon density
$k_{t,pow} = 0.1 \frac{W}{m K}$	Powder nylon thermal conductivity	$c_p = 1363 \frac{J}{kg K}$	Specific heat
$k_{t,liq} = 0.3 \frac{W}{m K}$	Liquid nylon thermal conductivity	$L_f = 3.7875E7 \frac{J}{kg}$	Latent heat of fusion
$h_t = 30 \frac{W}{m^2}$	Heat transfer coefficient	$\epsilon = 0.9$	Powder nylon emissivity
$\sigma = 5.67E - 8$	Stefan-Boltzmann constant	$R = 0.6$	Powder reflectivity
$T_{sol} = 458 K$	Solidus temperature	$\beta = 2E4 \frac{1}{m}$	Extinction coefficient
$T_{liq} = 468 K$	Liquidus temperature	$T_A = 453 K$	Ambient Temperature

Table 2.2 Standard parameters for nylon SLS used in finite volume analysis

The first situation that was evaluated was to measure the rough order of magnitude of the heat transfer paths. This was done by running a simulation with 6 watts of laser power, then repeating that same simulation while ignoring any conductive, convective, and radiative heat transfer (other than the laser radiation source). Comparing the results of the two simulations reveals less than 1% difference in the maximum temperatures [63]. This means that at the time scale of the laser-material interaction, conductive, convective, and radiative heat loss can be neglected with minimal error. If these heat losses are

ignored in equation 2.1, the model can be simplified significantly to equation 2.3.

$$T(t) = T_0 + \frac{Q}{\rho c_p} t \quad \text{EQ 2.3}$$

Equation 2.3 shows that the temperature increase ( $T-T_0$ ) is independent of the initial powder temperature  $T_0$  and is solely dependent on laser energy and time, assuming the material properties are constant within this temperature range. This implies that using a fixed laser power and speed will result in a constant temperature increase and by controlling the laser energy being deposited, the maximum post-sintering temperature can be controlled. While this equation does not take into account the latent heat of fusion, the conclusion still holds if it is assumed that all powder undergoes the same amount of phase change during laser heating. This result is significant because it reveals a simple relationship between temperature change and laser power that can be exploited when developing the laser power controller.

While ignoring heat loss yielded sufficient results for evaluating maximum temperature achieved by the powder, it clearly will not work when evaluating how the temperatures in the powder evolve over time. As such, it is also necessary to run simulations utilizing the full model described in equation 2.1. One question the model may be able to answer is what happens to the quality of melt when a temperature gradient exists on the powder bed.

To predict temperature and melt distribution in a real world build environment, a simulation was run where the pre-sintering temperature was non-constant. To simulate the temperature gradients caused by SLS bulk powder pre-heat systems, a linear temperature gradient was applied to the initial conditions, varying in temperature along the scan vector, while keeping the temperature constant in the z-direction. This is seen

visually in figure 2.2(a) where the top of the image is the top surface of the powder, moving down the image represents increasing depth into the powder bed and the image is of a plane that is collinear with the laser scan vector. The initial conditions of the melt percent of the powder show 100  $\mu\text{m}$  of virgin powder resting on top of a section of fully molten nylon, as seen in figure 2.2(b). This represents the case of building successive layers on top of each other, where fresh powder has been spread over nylon that was fully melted on the previous layer. The critical piece of information to look at in the results of the simulation is the melt profile of the newly sintered material.



Figure 2.2 Initial conditions of thermal simulation showing a side view of (a) starting temperature and (b) starting melt fraction

After being sintered with a constant 5 watts, the melt fraction was examined and presented in figure 2.3. As can be seen, on the left side of figure 2.3 where the initial powder temperature was higher, the laser caused the entirety of the new layer to melt and create a strong bond with the previous layer. On the right side where the pre-sintering temperature was just a few degrees lower, the melt percent of the powder at the interface

is as low as 50%. This is undesirable as it means the new layer of powder did not fully bond to the previous, resulting in a weak spot. The thermal conditions of this simulation are common in industrial SLS machines and can be a potential cause of the inconsistent and position-dependent strength of parts.



Figure 2.3 Melt fraction when applying a constant laser power to powder with non-constant temperature

One potential solution is to simply increase the laser power globally to a point that would ensure the lowest temperature powder on the new layer would fully melt. There are a few issues with this approach, however, as this would preserve whatever temperature gradients are initially present in the powder. Preserving these temperature gradients will typically contribute to dimensional inaccuracies such as curl and over-sintering where temperatures were initially high. Also, in areas where pre-sintering temperature was high, this will lead to adding more energy than necessary to get full melt and could potentially start to degrade the polymer if too much energy is used.

An alternative solution is to vary the laser power, increasing its intensity where the powder is colder. This allows for a homogenous melt depth without exposing powder to unnecessary risk of over-sintering. The same simulation as above was repeated, now using a linearly increasing laser power to account for the decreasing powder temperature. The power started off at the same 5 watts used previously, then linearly increased to 6 watts through the length of the vector. The post-sintering melt fraction results are given

in figure 2.4. As can be seen, the right side of the melt now shows that the new layer of powder was fully bonded with the layer below it.



Figure 2.4 Melt fraction when applying a variable laser power to powder with non-constant temperature

The simulation results show that the current method of utilizing a pre-defined, fixed laser power in SLS produces sub-optimal results that can lead to poor component consistency. They also show that it is possible to improve the results through more intelligent control of the laser intensity.

## Chapter 3: Laser-Polymer Interaction

This chapter will discuss experimental methods and results for measuring how nylon powder reacts to laser radiation. It will also present findings from a proof-of-concept laser power controller capable of modulating laser power on single vectors.

### 3.1 TEMPERATURE MEASUREMENTS

In order to develop a laser control method, it is imperative to understand how laser power affects temperatures on the powder surface. This section will detail empirical measurements made on the LAMPS SLS machine.

One of the unique features of LAMPS is its infrared imaging capabilities. In order to achieve high-fidelity thermal measurements, a FLIR SC8240 high-speed MWIR camera is directed through a dichroic prior to the laser galvanometers. This aligns the field of view of the SC8240 camera coaxially with the laser. The result is a stream of 64x64 pixel images recorded at 2,243 Hz with the laser spot always in the center of the image. The spatial calibration is such that each pixel width is approximately 300  $\mu\text{m}$  on the powder surface. An example of the data recorded by the SC8240 camera is shown in figure 3.1. This figure shows a sub-optimal velocity compensation tuning, something unable to be precisely measured without the use of a bore sighted IR camera. Velocity compensation is a tuning parameter available on the EC1000 control board that controls laser power to compensate for changes in galvanometer velocity. The galvanometers have a finite mass and are incapable of changing velocity instantaneously, meaning the beginning and end of vectors have an acceleration period. If the laser power is set to a constant value during the acceleration period, more energy is deposited in these ends of vectors and the powder is heated more than the rest of the vector. This phenomenon is known as end of vector over-sintering and can cause a build to be unsuccessful.

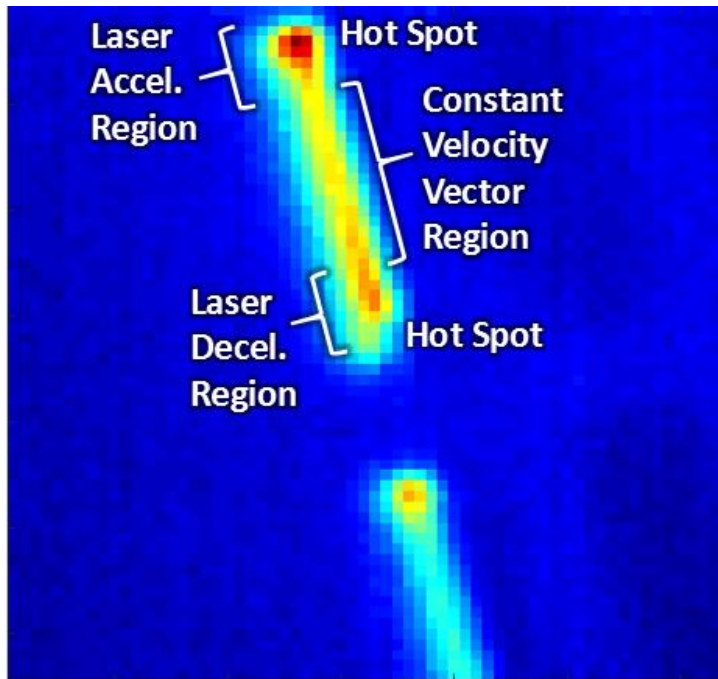


Figure 3.1 Thermal measurement from FLIR SC8240 camera

The relationship between laser power and temperature was evaluated using the SC8240 camera to measure the pre- and post- sintering temperatures of a vector. Figure 3.2 shows the pre-sintering and post-sintering temperatures when using 10% laser power. The second subplot is the same data with the pre-sintering temperature shifted linearly upward to coincide with the post-sintering temperature. It is clear from this measurement that the post-sintering temperature gradient mimics the pre-sintering temperature gradient. Figure 3.3 shows the same data for 45% laser power and yields the same result. Figure 3.4 shows similar data, but for a line that was split into two parts with a different power for each part. Again, the figure shows that at both power levels, the post-sintering temperature mimics the pre-sintering temperature. After more, similar tests, it is concluded that using a constant laser power preserves pre-sintering temperature

gradients. These results agree with the analysis in Chapter 2 that led to the simplified thermal equation 2.3.

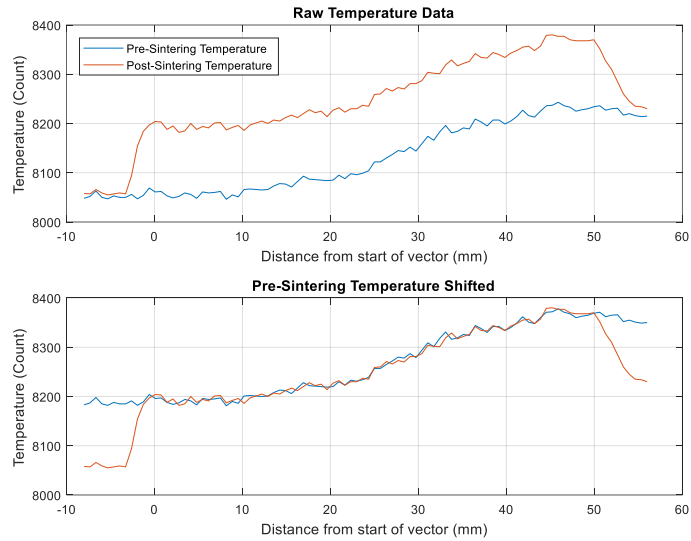


Figure 3.2 Pre- and Post-sintering temperature comparison with 10% laser power

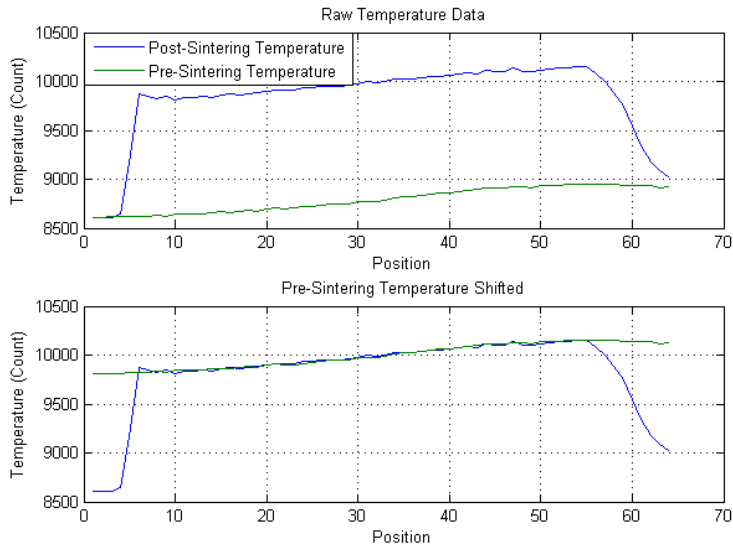


Figure 3.3 Pre- and Post-sintering temperature comparison with 45% laser power

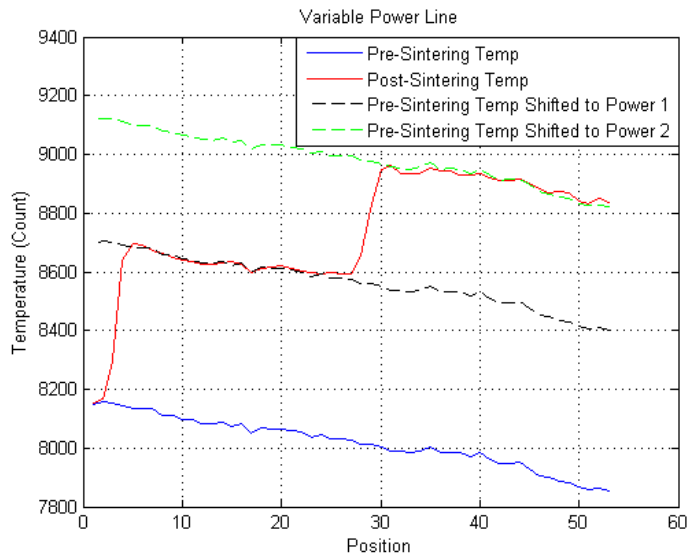


Figure 3.4 Pre- and Post-sintering temperature comparison with stepped laser power

The next experiment involved sintering vectors with different laser power percentages and comparing the pre-sintering and post-sintering temperatures. Powers of 5% to 50% were tested in 5% increments, with 4 tests performed at each power percentage. The test consisted of using the galvanometers to scan the bore sighted MWIR camera over the scan line to record the initial temperature profile, then the galvanometers scanned the same region using that test's fixed laser power. The data was analyzed and the average temperature increase for each scan line was determined. One of these trials, where laser powers of 5%, 10%, 15%, 20%, and 25% were tested, is given in figure 3.5. The average temperature increase for each test is shown in figure 3.6 with the difference between the pre-sintering temperature and the post-sintering temperature shown on the y axis and the laser power shown on the x axis with a 4th order polynomial fit to the data. At the 15%, 20%, and 25% laser power tests there was one outlier value each. These values were recorded on the first test of those percentages and it was decided that these were questionable data points and they were to be excluded when

making the laser power to temperature increase transfer function. The curve fit to the remaining data had an  $R^2$  value of 0.9988 and was used in subsequent testing as the laser power to temperature increase transfer function.

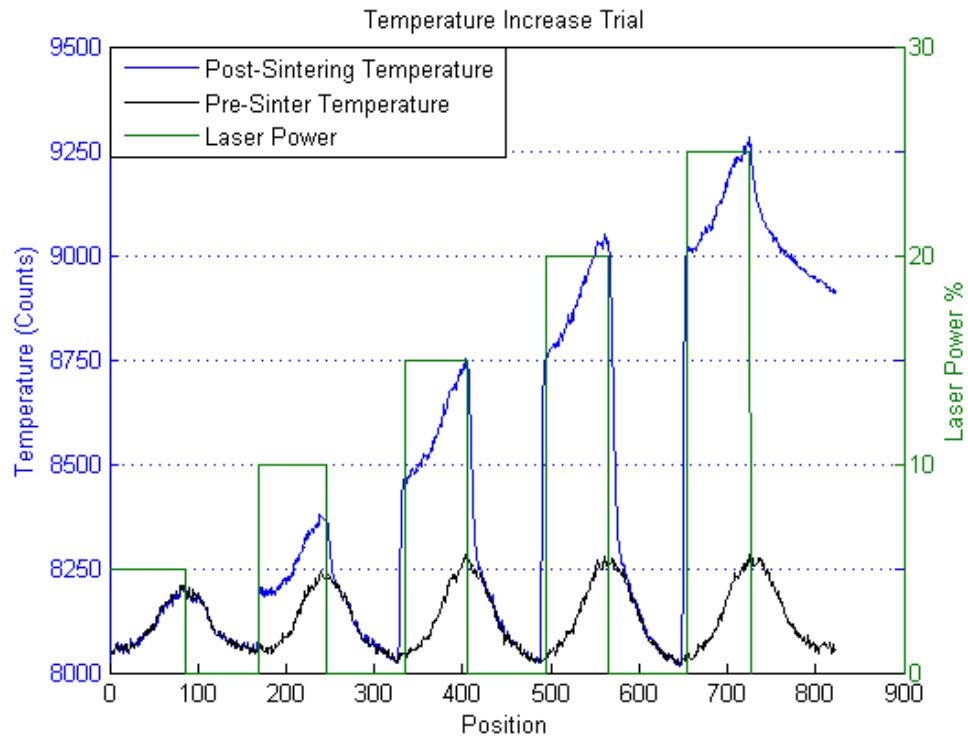


Figure 3.5 Multiple vectors showing laser power and temperature increase

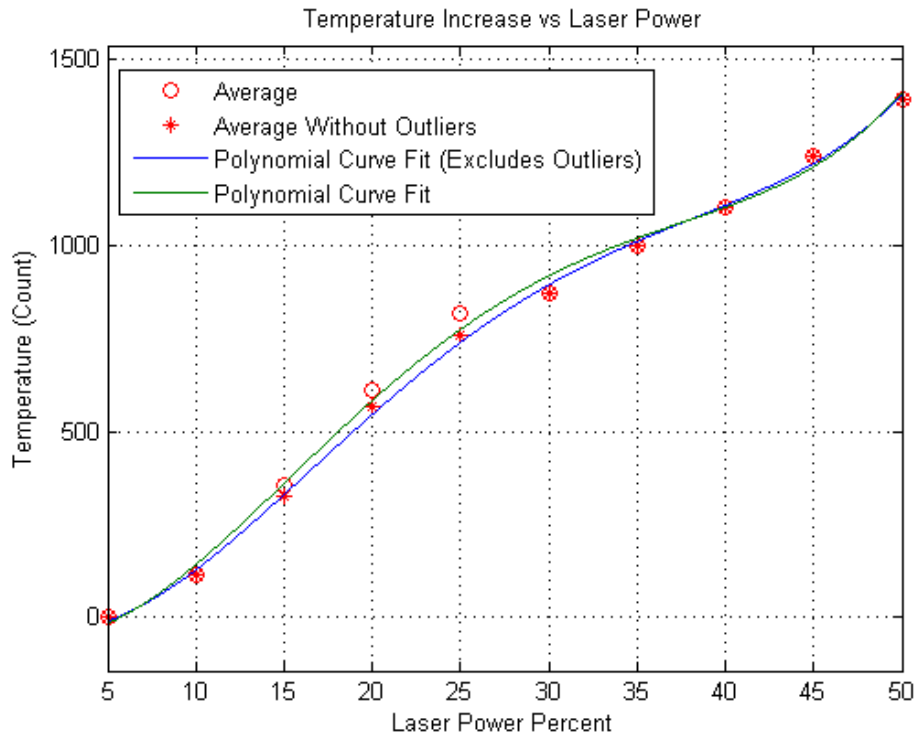


Figure 3.6 Single vector transfer function for laser power to temperature increase

### 3.2 LASER POWER MODULATION

The initial proof-of-concept test for temperature-dependent laser power modulation was to attempt to control post-sintering temperature over the length of a single vector. The first step towards accomplishing this was to use the SC8240 MWIR camera to measure the pre-sintering temperature of a vector. This temperature vector was fed through an algorithm that split the vector into subsections and assigned each one an optimal laser power based on its initial temperature, desired post-sintering temperature, and the transfer function found in figure 3.6. The SC8240 was used again during the sintering of the subsections to record the post-sintering temperature and verify that the control goal was achieved.

The algorithm for splitting the vector into subsections must weigh the competing objectives of achieving small temperature error while not producing an excessive number of subsections. In theory, the subsection lengths can be reduced to the length of a single pixel on the MWIR camera, effectively turning the laser into a pulsed source that delivers the exact amount of energy to raise each voxel of powder to the desired temperature. This will drive the error between the actual and desired post-sintering temperature to zero, but is likely not be the most effective means of in-situ control. There are a number of disadvantages to this method, including increasing the computation time and difficulty. For the high resolution MWIR camera, this method can result in hundreds of thousands of temperatures per layer that need to be analyzed. Another disadvantage is that any amount of error in the laser power control or velocity compensation will be compounded and lead to a poor thermal profile of the build surface.

An acceptable tradeoff between computation time and temperature control precision came from limiting the laser power percent to integer values. This creates a dynamic subsection spacing where a new subsection is created once the predicted temperature of the previous subsection reaches a certain limit. An example result of this dynamic subsection method is seen in figure 3.7. This method produces a relatively small error between the desired post-sintering temperature and the theoretically obtainable post-sintering temperature, while not adding significant time to the build.

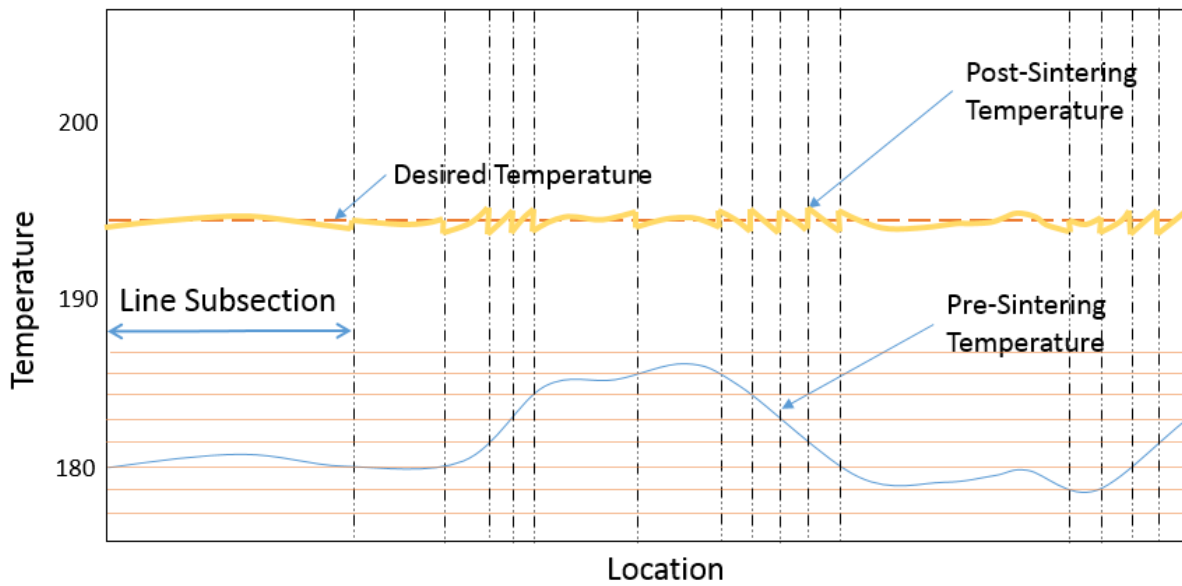


Figure 3.7 Simulated results from dynamic sectioning algorithm

### 3.3 RESULTS AND DISCUSSION

In-Situ control of vector-level laser power was performed as specified in section 3.2 with the results presented here. The pre-sintering temperature profile for one of the trials is seen in figure 3.8. The first subplot shows the raw temperature data from the pre-scan with the first 340 and the last 1100 frames being dwell time for the galvanometer. The second subplot shows a close-up of the non-dwell time region which is the temperature profile of the scan line. This temperature is fed through the laser power to temperature increase transfer function with a desired post-sintering temperature of 9000 Counts. The resulting laser power profile is seen in figure 3.9. The galvanometer position coordinates for the scan line are 11 – 46. As you can see, the scan line was split into 13 subsections, each with its own length and laser power percentage based on the pre-sintering temperature profile.

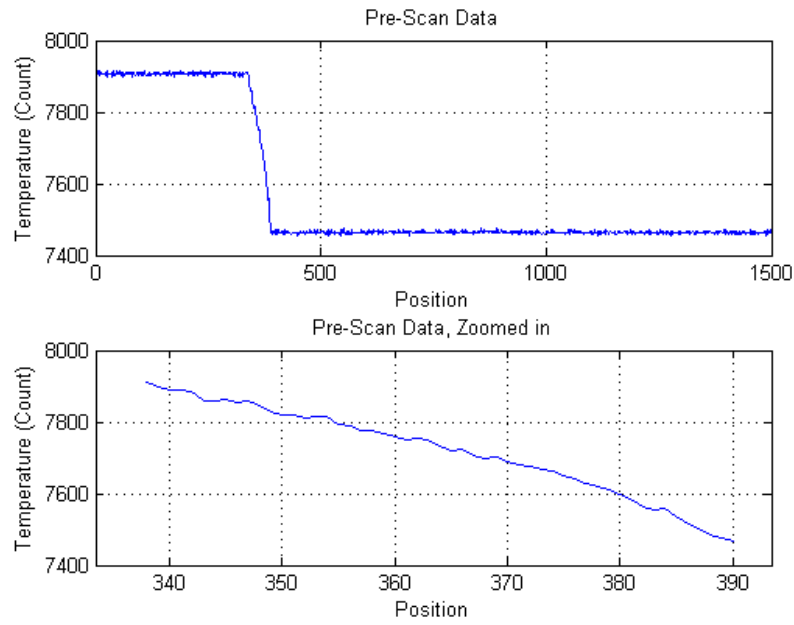


Figure 3.8 Pre-sintering temperature profile for in-situ vector power control

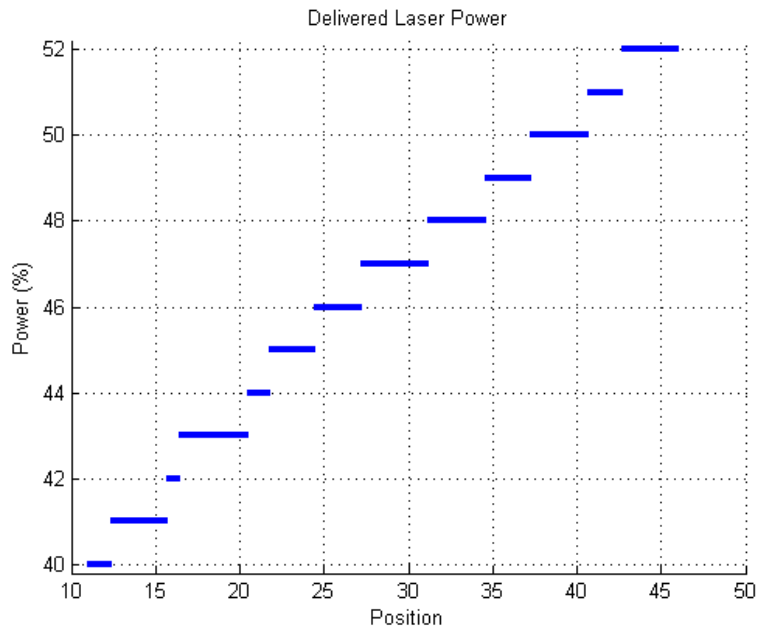


Figure 3.9 Optimal laser power of dynamically sectioned vector.

The vector pre- and post-sintering temperatures after executing the optimal power vector are found in figure 3.10. In this figure, the red line shows the pre-sintering temperature that was fed through the laser control algorithm and used to determine the subsection laser power profile. The process to analyze the pre-sintering temperature, create a scan file, and implement the laser control took roughly 2 minutes, so the pre-sintering temperature was re-measured immediately prior to sintering to determine the extent to which the system has changed in the time since the initial data was taken. The re-measurement of pre-sintering temperatures is shown in blue. If the blue line was significantly different than the red line, it would be expected that the in-situ control would not perform as expected, as the control was based off a representation of the system that was no longer accurate. The black line is a prediction of the post-sintering temperature determined by feeding the commanded laser power values back through the laser power transfer function. The green line is the measured post-sintering temperature, which is centered on the desired temperature of 9000 Counts. If the in-situ control strategy is working correctly, this line should match closely with the black line, the expected post-sintering temperature. This result shows that the post-sintering temperature was successfully controlled and was not influenced by the pre-sintering temperature gradient.

The trial depicted in figure 3.10 performed exceptionally well and showed that a high level of temperature control is possible with the method proposed. The results of all in-situ control trials are summarized in table 3.1. As can be seen from the “Temp Range Decrease” and the “Temp STD Decrease” columns of table 3.1, all of the trials exhibited a post-sintering temperature profile that was superior to the pre-sintering temperature in terms of uniformity. This cannot be said of the baseline trials, whose post-sintering temperature profile mimicked the pre-sintering profile.

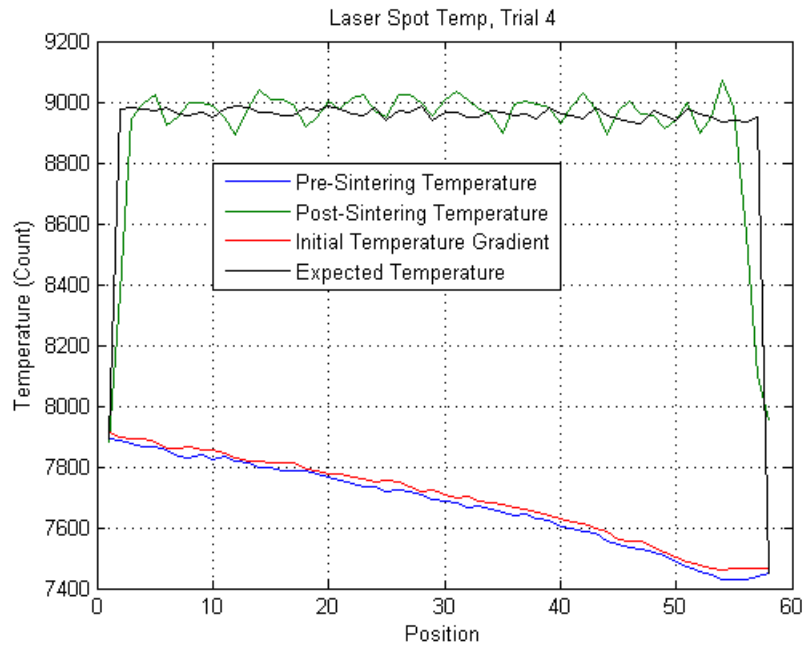


Figure 3.10 In-situ vector-level control results

Trial	Avg. Pre-Sintering Temp.	Pre-Sintering Temp Range	Pre-Sintering Temp STD	Avg. Post-Sintering Temp	Post-Sintering Temp Range	Post-Sintering Temp STD	Temp Range Decrease	Temp STD Decrease
1	762	457	142.2	8482.8	389	89.28	14.88%	37.22%
2	762.2	402	126	9083.6	210	41.91	47.76%	66.74%
3	8018.4	326	96.6	8901.6	149	31.5802	54.29%	67.31%
4	7682.4	439	124.5	8978.1	183	40.8	58.31%	67.23%
5	7768.9	377	114.6	9042.1	245	68.4	35.01%	40.31%
6	7677.3	374	110.2	9292.4	250	52.9	33.16%	52.00%
7	7663.7	396	112.2	8953.3	191	45.3	51.77%	59.63%
8	7610.4	385	114.8	8988.2	258	60.9	32.99%	46.95%
9	7575.1	391	116.4	8931.2	303	79.8	22.51%	31.44%
10	7745	355	103	8761	124	24.2	65.07%	76.50%

Table 3.1 Results of vector-level power control

The results of vector-level testing are overwhelmingly positive, with each test outperforming the baseline control method. Temperature variations throughout a scan line were shown to be greatly diminished when using the in-situ control method employed. The effect of the pre-sintering thermal profile on the post-sintering temperature was reduced up to 65%. This increased control over laser energy deposition and the corresponding decrease in post-sintering temperature gradients is advantageous for creating high-quality components via Selective Laser Sintering. By decreasing the thermal gradient in the post-sintering part, it is believed that the mechanical and dimensional properties of the part will be improved [64]. Using the same strategy, multiple scan lines can be controlled and stitched together to form cross-sections of the component whose temperature uniformity is much greater than if the traditional, fixed power control method was used.

Though this initial control method showed promise, there were limitations and opportunities for improvement identified. The time it took to create optimal laser power vectors was unreasonably long due to the amount of operator input required. This process will need to be fully automated and the calculation time significantly reduced in order to apply to successive scan lines and areas. Also, the exact galvanometer position was not measured, but was inferred from knowing scan speed and vector locations. This could potentially result in spatial errors of temperature measurements as the galvanometers moved across the powder bed. The subsequent chapters will address these issues and detail the next steps of expanding this feedforward concept to improve temperature control over an entire build.

## **Chapter 4: Component-Level Laser Power Control for Simple Geometries**

This chapter will build on the findings of the previous chapter to turn the vector-level power controller into a fully automated component-level power controller. Multiple control methods will be presented along with thermal and mechanical testing results. Inadequacies in the lookup table approach introduced in Chapter 3 will be highlighted and a dynamic surrogate model-based controller will be introduced to address them.

### **4.1 CONTROLLER DESIGN**

Multiple control theories were evaluated in an effort to develop a fully automated laser control system, all with the same goal of homogenizing post-sintering temperatures. The controllers in this section were required to work within the hardware constraint of the LAMPS machine at the time, meaning galvanometer position feedback was unavailable and each vector must have a predetermined, constant power. Since real-time galvanometer data was unavailable, it would not be possible to precisely know the field of view of the bore sighted SC8240 camera. For this reason, the controllers presented in this chapter will instead utilize a FLIR A6701 MWIR camera mounted in a fixed location to provide thermal feedback. This camera records 640x512 pixel images at a framerate of 60 Hz and is directed onto the build surface through a Zinc Selenide window.

The A6701 MWIR camera records video during the sintering process and, for each layer, condenses the video into a single frame showing the maximum value each pixel recorded during that layer. This frame is known as the composite max post-sintering temperature and is used as the thermal feedback to build the control models. This temperature is not exactly equal to the highest temperature experienced by the powder, but is the highest temperature recorded with the A6701 MWIR. Aliasing due to

the relatively slow framerate of the camera makes it so these numbers are not equal, but this composite max post-sintering temperature is still useful for comparing temperatures. It is this composite max post-sintering temperature that is to be homogenized throughout the build. Other frames of interest generated by the A6701 MWIR are the pre-sintering temperature taken just prior to the commencement of sintering, and the measured temperature increase, which is the subtraction of the pre-sintering temperature image from the composite max post-sintering image.

#### **4.1.1 Immutable Empirical Model**

The first attempt at component-level power control uses a so-called immutable empirical model. The immutable empirical model approach is similar to the transfer function approach taken in Chapter 3, extended to provide laser control over an entire layer. Instead of splitting each vector into subsections, this technique split each layer into its components and applied a fixed laser power to each component. Prior to building, an empirical model relating temperature rise with laser power is built. This model is then used on all subsequent layers to predict the optimal powers used in each component.

In order to build the laser power model, patches are sintered across the build chamber using varying powers ranging from 20% to 100% in each patch location. The composite max post-sintering images for each calibration layer are evaluated and the temperature rise within a sintered area is extracted and correlated with the laser power used. The results for all 30 rectangular locations are shown in figure 4.1. Rather than averaging all locations together to form one overall transfer function, each location is considered separate to account for non-uniformities in the laser window transmittance.

After the model is calibrated, the build commences. Each layer during the build process begins by capturing a thermal image prior to sintering. This data is analyzed and

used to determine the average temperature within each individual component to be sintered. These temperatures are each compared with a desired post-sintering temperature and the immutable empirical model is used to determine the optimal laser power in each component. Once these optimal powers are found, the build file that describes the scan geometry is split into as many sub-files as there are components. Each sub-file depicts all the laser commands associated with a single component and is prepended with the corresponding optimal laser power. These files are sent to the laser controller, which sinters each component before a new layer of powder is spread and the process is repeated. For each component, laser power is constrained to only change between layers and not on the interior of a component, making this technique not capable of as fine temperature control as the vector-level control introduced in Chapter 3; however, this constraint greatly reduces the complexity.

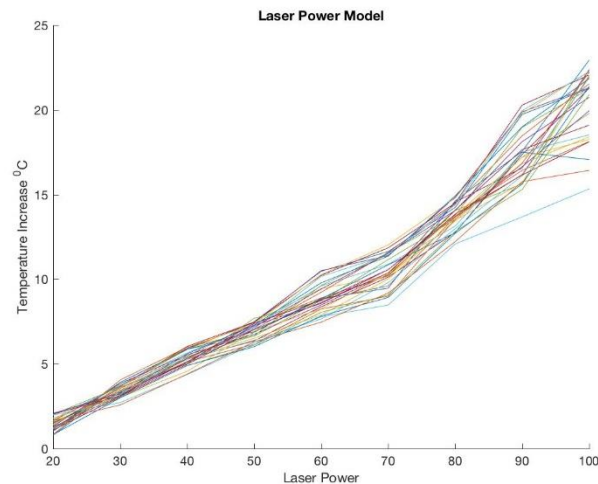


Figure 4.1 Temperature increase vs laser power transfer function for various positions in the powder bed

In order to test this controller, a build was designed that consisted of 30 rectangles similar in cross-section to z-axis tensile specimens. This build was run using both a fixed laser power, to provide baseline results, and using the immutable empirical model described above. During the builds, LAMPS was controlled in a suboptimal way to produce a larger-than-typical temperature gradient of 15-20 °C. This was done to stress test the control method by exposing it to extreme conditions. An example baseline composite max post-sintering image is given in figure 4.2(a). While it is obvious in figure 4.2(a) that the post-sintering temperatures are not consistent, the extent of which is somewhat lost. In order to display this more clearly, a single row of 10 rectangular components is isolated and plotted in figure 4.2(b), with the y-axis representing temperature and the x-axis representing the same x-direction on the powder bed. At first glance, this data seems to not agree with the results from chapter 3 that a fixed laser power produces a constant temperature increase, as the first 3-4 sintered regions appear to have larger temperature increase than the others. However, the pre-sintering temperature gradient was so great in this test that after laser scanning, the regions in the colder portion of the powder bed did not fully melt. Since melting consumes energy to overcome the latent heat of fusion, it is reasonable to expect powder that does not fully melt to experience a greater temperature increase. As the pre-sintering temperature increases (moving right in figure 4.2(b)), the powder undergoes more melting, thus decreasing the temperature rise until the powder within the sintered region fully melts and the temperature increase is constant.

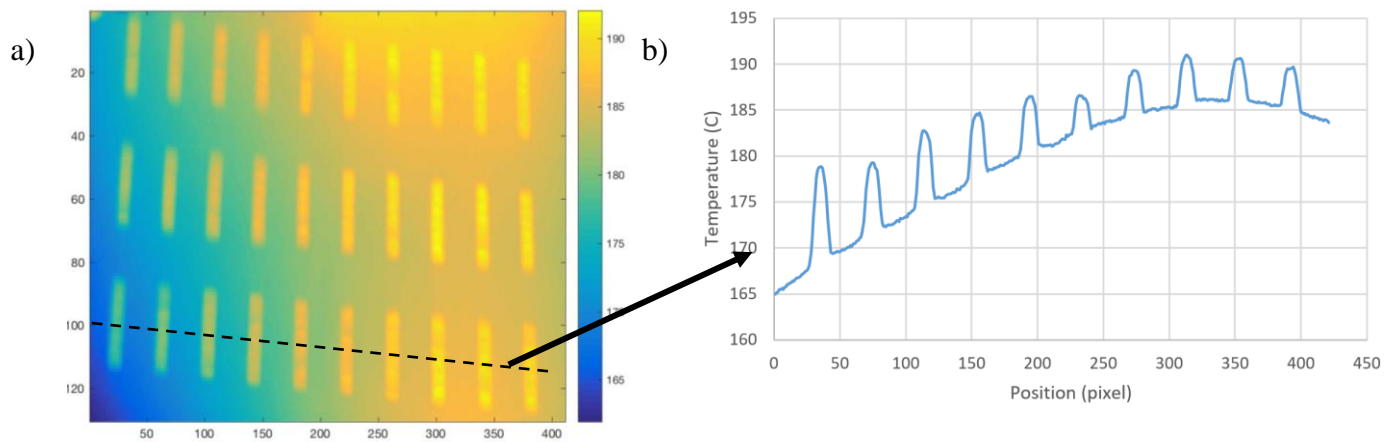


Figure 4.2 Baseline results for non-controlled laser sintering showing (a) a composite max post-sintering image and (b) the temperature profile along the vector indicated

The build was repeated using the laser control technique and immutable empirical model described above. After taking the initial powder temperature measurement, the optimal laser powers were defined and the layer was sintered accordingly. The laser power profile for one row of rectangular components can be seen in figure 4.3(a) and the resulting post-sintering temperatures in figure 4.3(b). In this test, the pre-sintering temperatures for the rectangular areas had a difference of 14 °C while the post-sintering temperatures have a difference of less than 4 °C. Further testing, though, showed unstable results. While the first few layers of a build using the immutable empirical model exhibited good temperature control, the post-sintering temperature began to deviate from its desired value as the build progressed. It is believed that changes in the machine throughout the build, such as transmittance changes in the optics [11], caused the static model's ability to predict temperature changes to degrade over time.

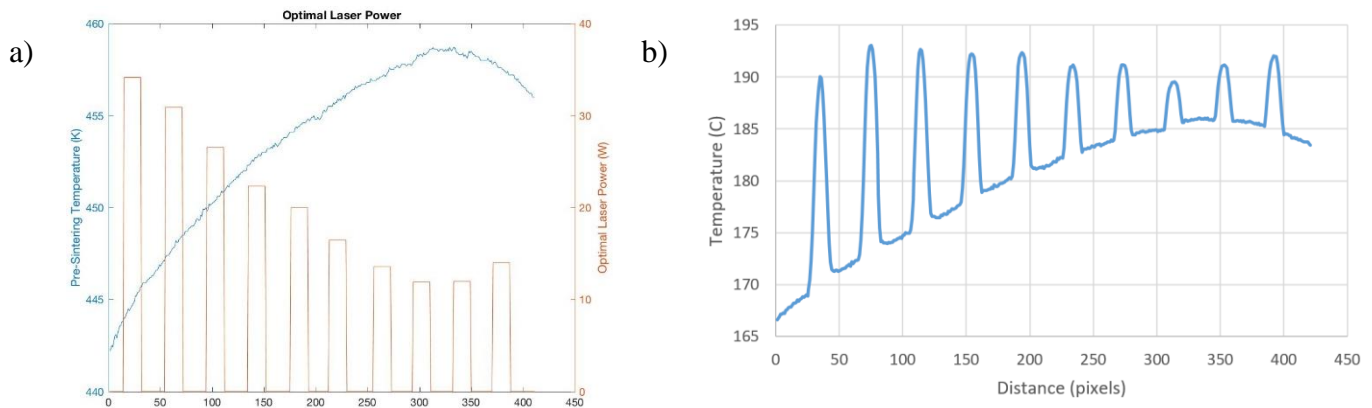


Figure 4.3 Results from using the immutable empirical model showing (a) the presintering temperature and calculated laser power profile and (b) the resulting post-sintering temperature profile

#### 4.1.2 Dynamic Surrogate Model

In order to overcome the deficiencies of the approach described above, a more complex model must be employed that can take into account changes that occur during the build process. Researchers in the past have worked to create physics-based models of the sintering mechanics in SLS, but these typically use numerical solution methods and are not feasible to implement in this in-situ control process due to their slow speed [58] [65]. A more practical approach here is to continue using a feed-forward approach, but with a dynamic surrogate model that is built during runtime from real machine results. The proposed laser control technique is shown visually in figure 4.4 and consists of the following steps:

1. Use the FLIR A6701 MWIR camera to capture an initial dataset showing the pre-sintering powder temperature.
2. Compare the current, pre-sintering powder temperature within the build regions to a pre-defined optimal post-sintering temperature.
3. Use the dynamic surrogate model to translate the desired temperature increase to an optimal laser fluence for each component.

4. Actuate the laser according to the optimal laser fluence on each area of the powder bed and repeat steps (1)-(4) as needed until the layer is completed.
5. Use the A6701 images to create the composite max post-sintering image and extract average post-sintering temperature values for each component.
6. Update the dynamic surrogate model with the new temperature increase and laser power values.
7. After successful completion of a layer, spread a new layer of powder and repeat the process until all components are completed.

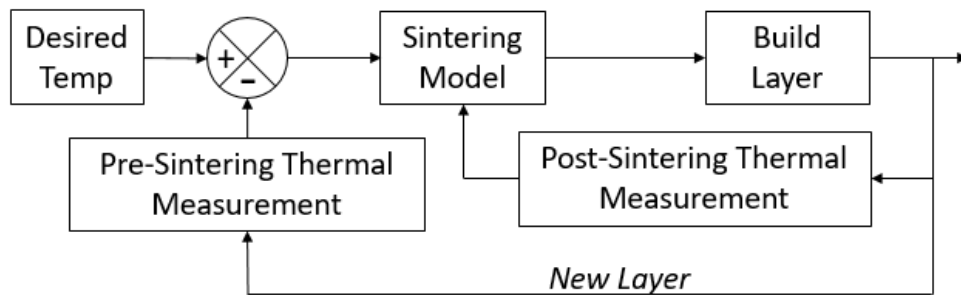


Figure 4.4 Dynamic surrogate model-based laser power controller block diagram

The dynamic surrogate model developed for this controller is built during runtime using thermal measurements of all previously completed layers. The controller considers each component to be a separate entity and, thus, builds an empirical model for each one in the build. After sintering each layer, the composite max post-sintering image is analyzed to determine the average temperature rise each component experienced. Since this controller is built for simple geometries, post-sintering temperature extraction is accomplished by simply extracting data at pixel locations that are known to correspond with the component locations. For each component, the commanded laser power and average temperature rise is added to the model to improve its predictive capabilities.

The thermal models use weighted least squares regression to fit a second order polynomial to the laser power and temperature rise data. The most recent data point has the highest weight in the fitting function because of its ability to predict the current machine state, while the weight of older data decays as new data points are added to the model. This effectively produces a forgetting factor that allows the thermal model to deviate from older data points that may no longer characterize the system. The result is a dynamically updated model that accurately represents the system throughout the entire build.

Since the model is built with real machine results during runtime, it will be accurate for any set of machine parameters (hatch spacing, scan speed, etc.) as long as those parameters are constant throughout the build. An example of one model built during runtime can be seen in figure 4.5. The red dots represent data recorded during the build process, with their size representing the weight of each measurement. The weights are not normalized, but can be thought of as relative confidence levels in each measurement. More recent data and boundary conditions imposed on the model are weighted more highly, with a maximum of 100, while older data has a lower weight, with a minimum of 2. The model is constrained to be monotonically increasing with the boundary conditions of: (1) A very high confidence that a laser duty cycle under the minimum threshold results in zero temperature rise and (2) a moderate level of confidence that 100% laser power results in a specific temperature rise value that was found experimentally.

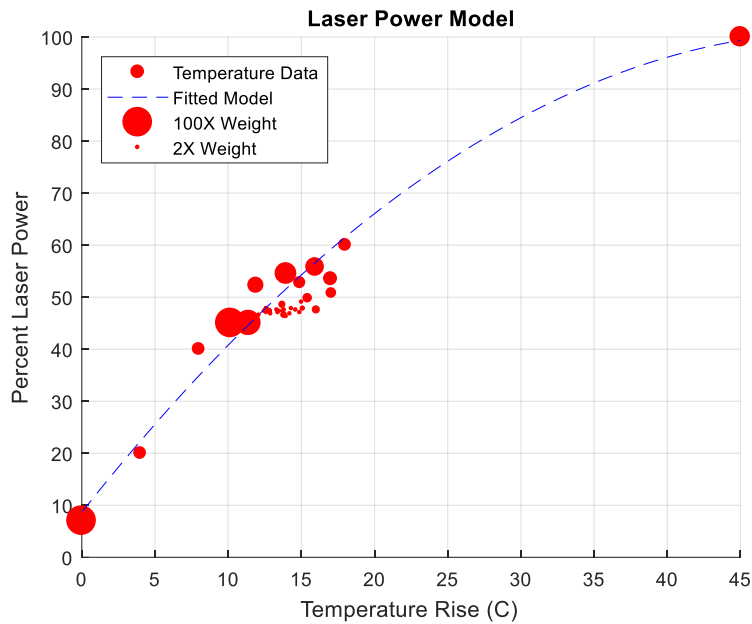


Figure 4.5 Example of a dynamic laser power model

## 4.2 EXPERIMENTS

Aside from the standard post-sintering temperature measurements, two additional experiments were conducted to evaluate the performance of the laser power controller. It is important to evaluate the thermal performance of the models, as this is the process variable; however, a more significant measurement for manufacturing purposes is the actual mechanical performance of the components. For this reason, flexural strength and percent crystallinity measurements were also performed.

### 4.2.1 Polymer Structure

Differential scanning calorimetry (DSC) was used to evaluate the structure of as-built nylon 12 samples. DSC is a widely used thermoanalytical technique used to evaluate, among other things, melting, heat capacity, enthalpy, and percent crystallinity in polymers [66] [67]. It is capable of measuring these properties by precisely controlling

heat flow into and out of a sample and measuring the sample's resulting temperature change. Equations 4.2-4.4 demonstrate how some of the critical polymer properties are calculated from DSC results. The process of calculating enthalpy is also shown visually in figure 4.6 for a sample of PET [68].

$$c_p = \frac{1}{m} \left[ \frac{\delta H / \delta t}{\delta T / \delta t} \right] \quad \text{EQ 4.2}$$

$$\Delta H_s = \int_{T_s}^{T_l} \left( \frac{dH}{dt} \right) dt \quad \text{EQ 4.3}$$

$$\% \text{ Crystallinity} = \frac{\Delta H_s}{\Delta H_{100}} \quad \text{EQ 4.4}$$

$m$  = Sample mass                       $c_p$  = Specific heat capacity                       $\delta H / \delta t$  = Heat flow  
 $\delta T / \delta t$  = Heating rate                       $T_l$  = Liquidus temperature                       $T_s$  = Solidus temperature  
 $\Delta H_s$  = Enthalpy of sample                       $\Delta H_{100}$  = Theoretical enthalpy of a 100% crystalline sample

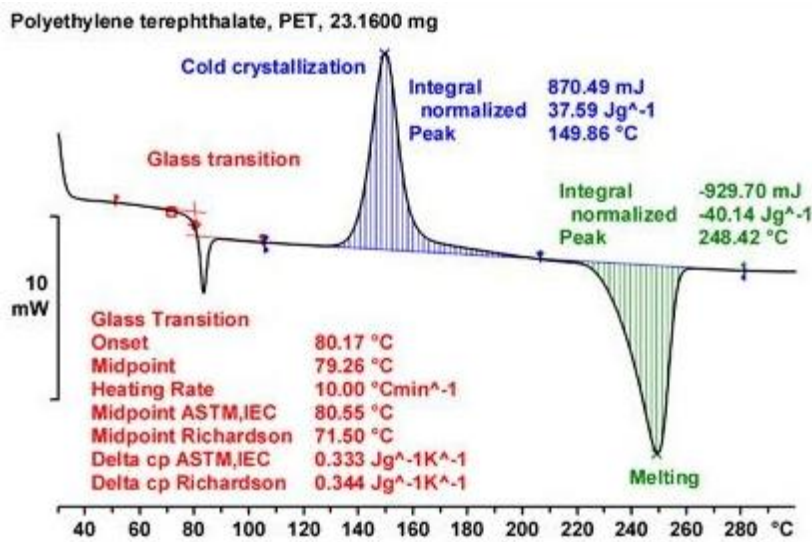


Figure 4.6 Example DSC results of PET demonstrating how to calculate enthalpy [68]

Percent crystallinity is an important property of semi-crystalline polymers as it influences stiffness, shear modulus, yield stress, density, and permeability [69] [70]. In powder processing applications, such as SLS, it can also be used to measure the degree of particle melt (DPM) [71]. Assuming percent crystallinity is known for virgin powder and for material with 100% DPM, the DPM for a component can be calculated by interpolation. Other researchers have measured these values to be 47% crystallinity for virgin powder and 25% crystallinity for material with 100% DPM [72]. In additive manufacturing, DPM is arguable more important than percent crystallinity as it is a direct measurement of powder consolidation. If a component has low DPM, the inter-layer bonding will be weak and the component will exhibit poor mechanical properties.

Some semi-crystalline polymers, such as polyamide, exhibit multiple-melting peaks when evaluated with DSC. The exact reasoning for multiple melting endotherm maxima is not known, but it has been postulated that the peaks correspond to melting portions of the substrate with different crystal structures [73] [74]. This phenomenon has been observed in SLS nylon 12 samples where it has been suggested that the lower temperature maxima corresponds to regions that were melted and crystallized during the SLS process and the higher temperature maxima corresponds to un-melted particle cores [71] [75]. This double melting peak phenomenon present in selectively laser sintered nylon 12 enables a second method of evaluating DPM. By measuring the relative heights of the two melting endotherm maxima, the ratio of recrystallized material to un-melted powder can be approximated [71]. An example DSC result showing the two melting peaks for nylon 12 is given in figure 4.7 [71].

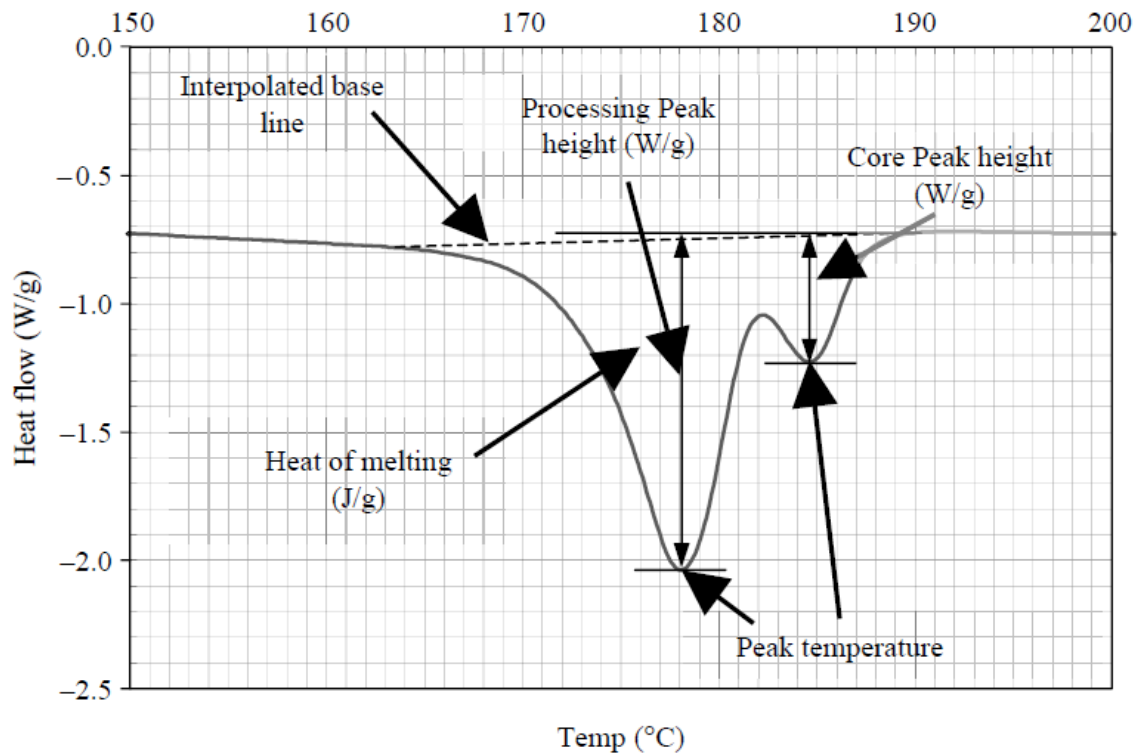


Figure 4.7 DSC results for nylon 12 showing the double melting peaks [71]

The builds for evaluating DPM consisted of 28 specimen measuring 10x10x2.5 mm<sup>3</sup> each. The laser control style, dynamic surrogate model-based laser power control or fixed laser power, was alternated in a checkerboard pattern. Post-processing involved shaving down all external faces of the components in order to remove any un-melted powder that was adhered to the sintered regions and to create samples of the correct thickness. Next, a punch was used to create cylindrical samples with a nominal mass of 5 mg as shown in figure 4.8. A LINKAM DSC450 optical DSC machine was used to heat the samples from 60 °C to 220 °C at a rate of 10 °C/min in accordance with ASTM testing

standard D3417 [76]. The associated LINKAM software and custom MATLAB scripts were used to evaluate the DSC results<sup>1</sup>.



Figure 4.8 Nylon 12 samples prepped for DSC

#### 4.2.2 Flexural Strength

To evaluate mechanical strength, flexure bars were built in groups of 10, split into two columns of five rows as seen in figure 4.9. Flexural strength was used as the testing parameter rather than the more common tensile strength due to the ability to create more flexural specimens in each build. The color and shade pattern in figure 4.9 depict which specimens were built using the same control method, with the control method alternating

---

<sup>1</sup> The author would like to acknowledge the Army Research Lab, Weapons and Materials Directorate for providing access to their LINKAM DSC equipment.

for each build. For example, on build 1, the green hatched bars used the automated laser controller (ALC) and the red dotted bars used a fixed power, then on build 2 the positions were swapped with each other. This alternating pattern helped ensure that neither controller was used in a preferential build location. A total of 11 builds over 3 days were completed, yielding 110 flexure specimens. Successive builds were separated with 1.5 mm of powder to minimize thermal influences. 10 specimens were identified to have been impacted by a powder feed issue during the build process and their data was disregarded. For all specimens, the scan speed was fixed at 1,500 mm/s with a hatch distance of 289  $\mu\text{m}$ , resulting in approximately 66% overlap of successive scan lines. A laser power of approximately 5.5 watts was used for all fixed power specimens. These parameters have been used previously with LAMPS and have been shown to produce high quality components.

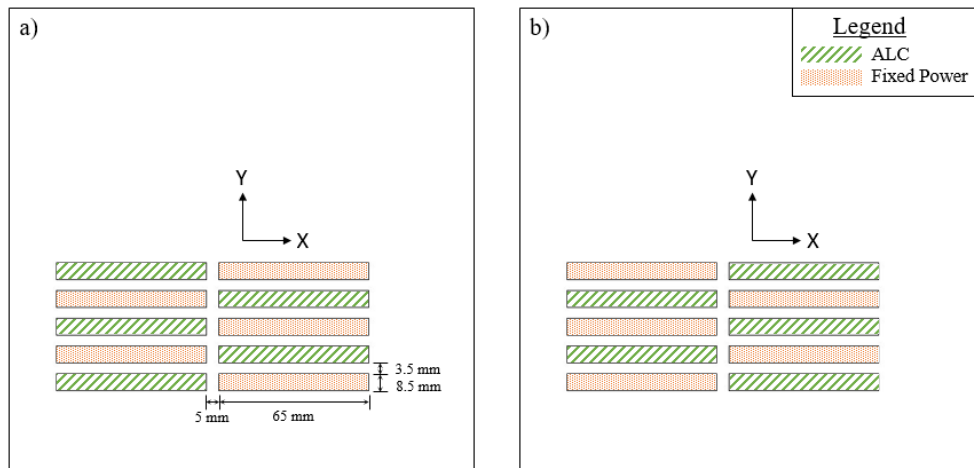


Figure 4.9 Flexure specimens build location and control pattern on (a) odd numbered builds and (b) even numbered builds

Each flexure specimen was tested in an Instron universal testing system in accordance with the ASTM D790 testing standard [77]. The specimens had a nominal size of 65 mm long x 8.5 mm wide x 3.5 mm thick. The testing support span was 50.3 mm and the crosshead motion rate was 12.05 mm/min. Prior to testing, loose powder was removed from each specimen and their dimensions were recorded and used to compute flexural strength according to equation 4.1, where P is load, L is support span, b is beam width, and d is beam depth [77].

$$\sigma_f = \frac{3PL}{2bd^2} \quad \text{EQ 4.1}$$

The flexure specimens were built and tested so that their thickness dimension was in the z-axis (i.e. each specimen was built using 35 layers, each 100 um thick to produce the 3.5 mm thick component). This testing direction places the maximum shear plane parallel to the layers so that inter-layer bonding has a large influence on the ultimate flexural strength measured [78]. Aligning the shear axis with the layer direction is desired because it is believed that poor inter-layer bonding is a common cause of weak components and is highly influenced by build parameters. An example of a weaker specimen delaminating during flexure testing is seen in figure 4.10, where delamination can be observed in the left half of the component.

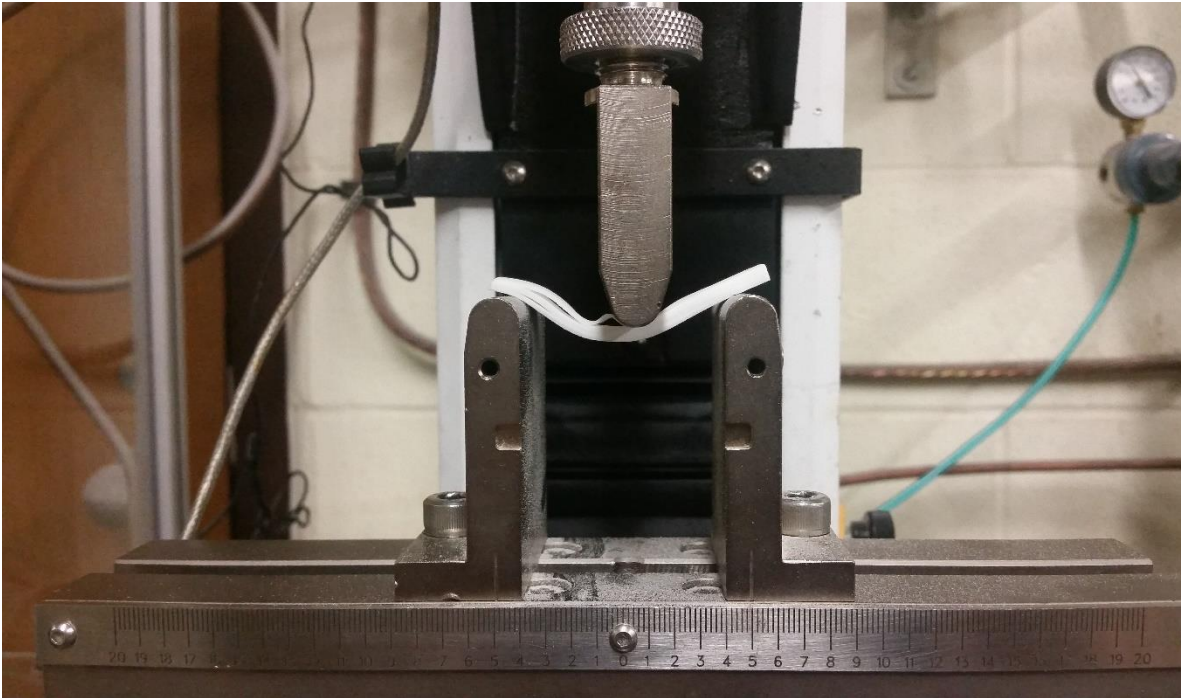


Figure 4.10 Flexure specimen delaminating under load

### 4.3 RESULTS AND DISCUSSION

The dynamic surrogate model-based laser power controller introduced in this chapter proved very successful in terms of increasing temperature uniformity. For one of the DSC sample builds consisting of 14 components built with a fixed laser power and 14 built using the automated laser controller (ALC), the ALC components displayed an approximate 48% reduction in post-sintering temperature range. The post-sintering temperatures can be seen in figure 4.11, where the blue data bars show the mean and range of the post-sintering temperatures of the laser-controlled components on each layer. The same data for the baseline, fixed power components is shown in red. As the build progresses, the temperature range of the laser controlled specimens becomes tighter as more data is collected and the dynamic surrogate model improves in accuracy. As is

expected, the baseline fixed power temperature range remains relatively constant throughout the build.

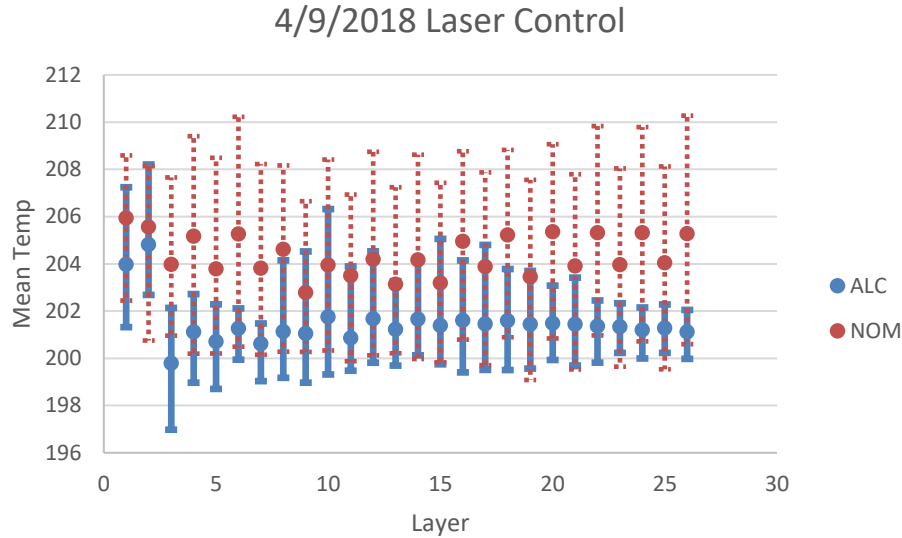


Figure 4.11 Temperature distribution for DSC samples

The temperature results from the flexure specimens showed similar improvements over temperature control. To measure the effects of the ALC controller, all specimens built using the same control technique were compared to produce the standard deviation between those components on each layer. For example, the post-sintering temperatures of the fixed power components had a standard deviation of 1.4 °C on layer 10, while on that same layer the post-sintering temperatures of the ALC components had a standard deviation of only 0.5 °C. Results from this analysis are shown in Figure 4.12. As can be seen, the post-sintering temperature standard deviation of ALC specimens started off similar to that of the fixed power components at layer 1. As the build progressed and the dynamic laser power model acquired more data, the results of the ALC components improved. Once the build had reached approximately layer 8, the standard deviation of the ALC components leveled out and averaged to a 57% improvement when compared to

the fixed power components, meaning post-sintering temperatures across the powder bed were much more uniform using ALC.

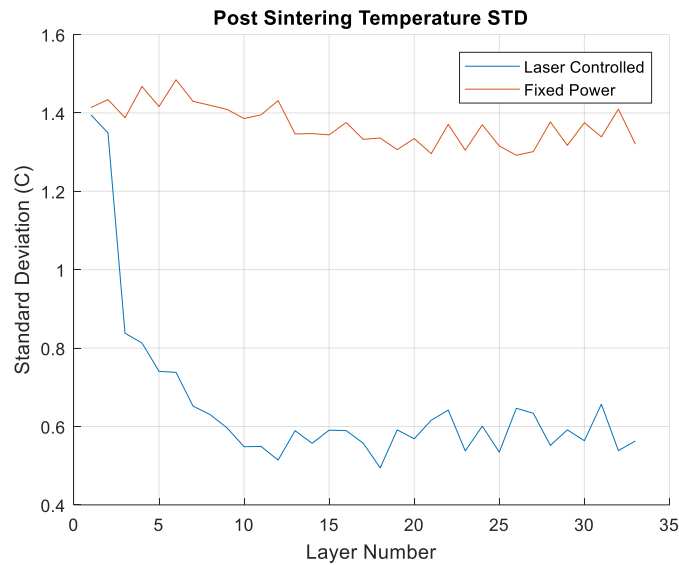


Figure 4.12 Temperature results from flexure specimens

Another visualization of the effects of the laser power controller is given in figure 4.13, which shows the average pre-sintering temperature and average laser power used for each component. The baseline results are obvious: a constant laser power was used regardless of the actual temperature of the powder. The ALC results show how the controller increased the laser power for components that were built in colder areas of the powder bed.

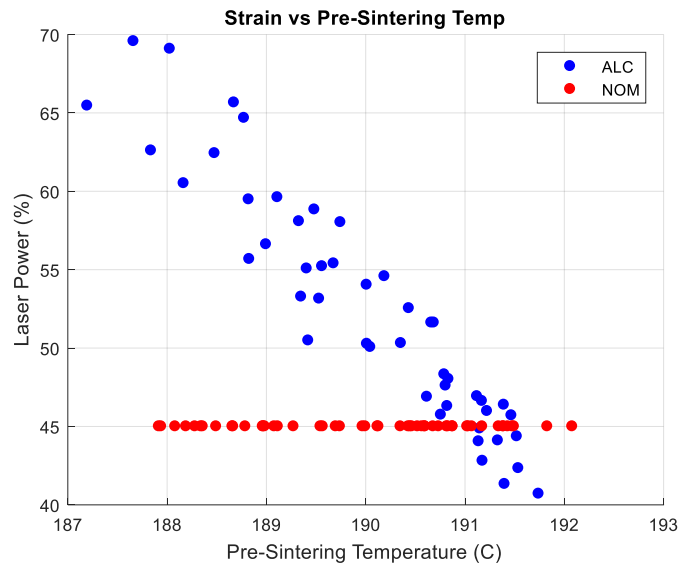


Figure 4.13 Laser power results from flexure specimens

Crystallinity and DPM results from the DSC experiments ultimately proved inconclusive. A data set from the DSC test showing heat flow vs temperature for a nylon 12 sample is given in figure 4.14. The data from the DSC test was evaluated using both methods described in section 4.2.1. However, when the enthalpies of the samples were compared, there appeared to be a correlation with sample mass, as seen in figure 4.15. Each sample mass was measured precisely and the LINKAM software should account for mass variation when determining enthalpy, so this correlation was not expected nor is it believed to be true. The likely explanation is that the DSC450 machine was not properly calibrated or was compromised in some way. Another explanation is that mass of the sample correlates with another property, such as sample height or surface roughness, that affects the DSC measurement and overshadows the potential differences created by the two control methods. Because of this unexplained phenomenon, no conclusions could be drawn from the DSC results.

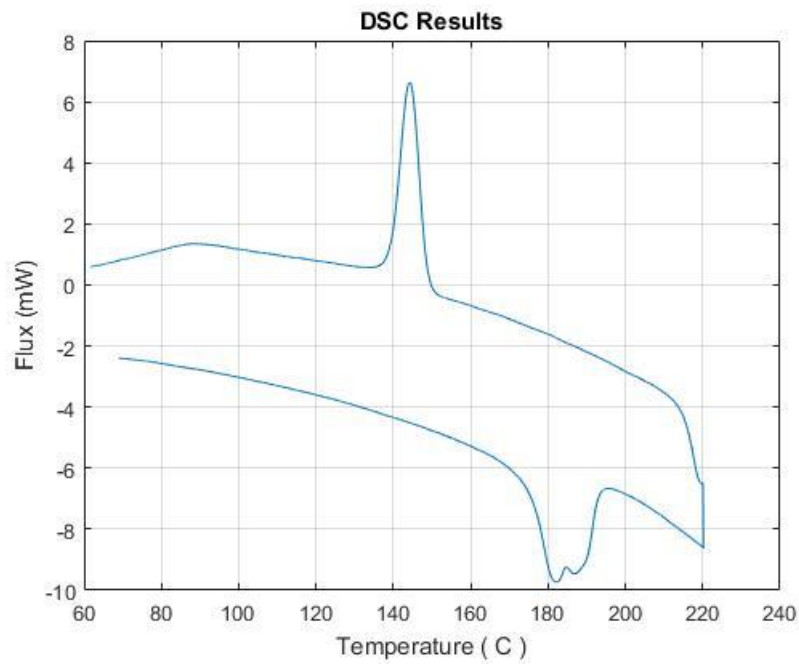


Figure 4.14 DSC curve for nylon 12 sample

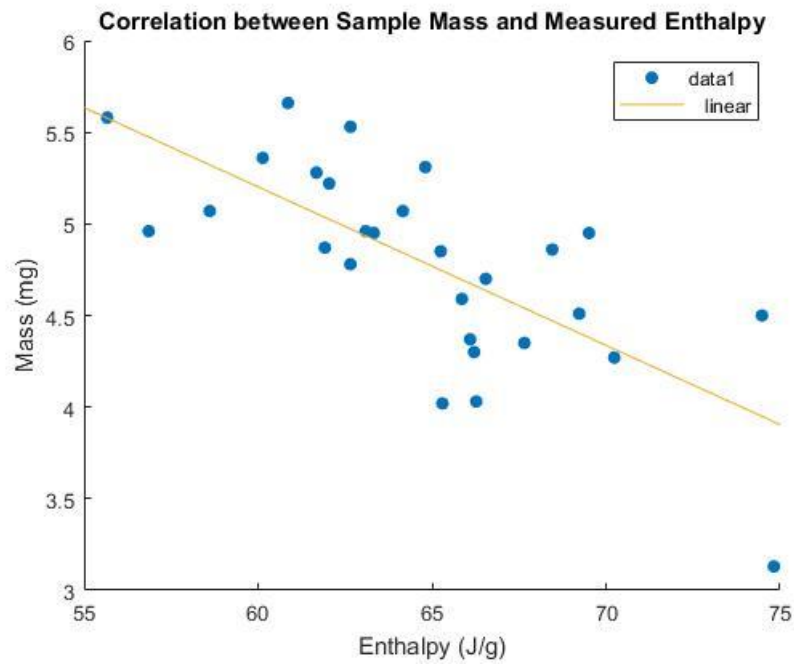


Figure 4.15 Correlation of enthalpy with sample mass

Although the percent crystallinity and DPM tests were inconclusive, the LINKAM DSC450 did allow for some interesting optical imaging of nylon throughout the melting process. Images taken as the DSC temperature ramped from 170 °C to 200 °C are given in figure 4.16. In figure 4.16(a) where the sample is still fully solid, you can see what appear to be particle cores as a lighter color surrounded by recrystallized material in a darker color. In figure 4.16(b), where the temperature is increased towards the first melting endotherm maxima, the regions believed to be the recrystallized material begin to melt. As the sample continues to heat up the material begins to fully melt and flow, as in figure 4.16(c) and (d). The molten nylon figure shows the level of porosity that the SLS process created.

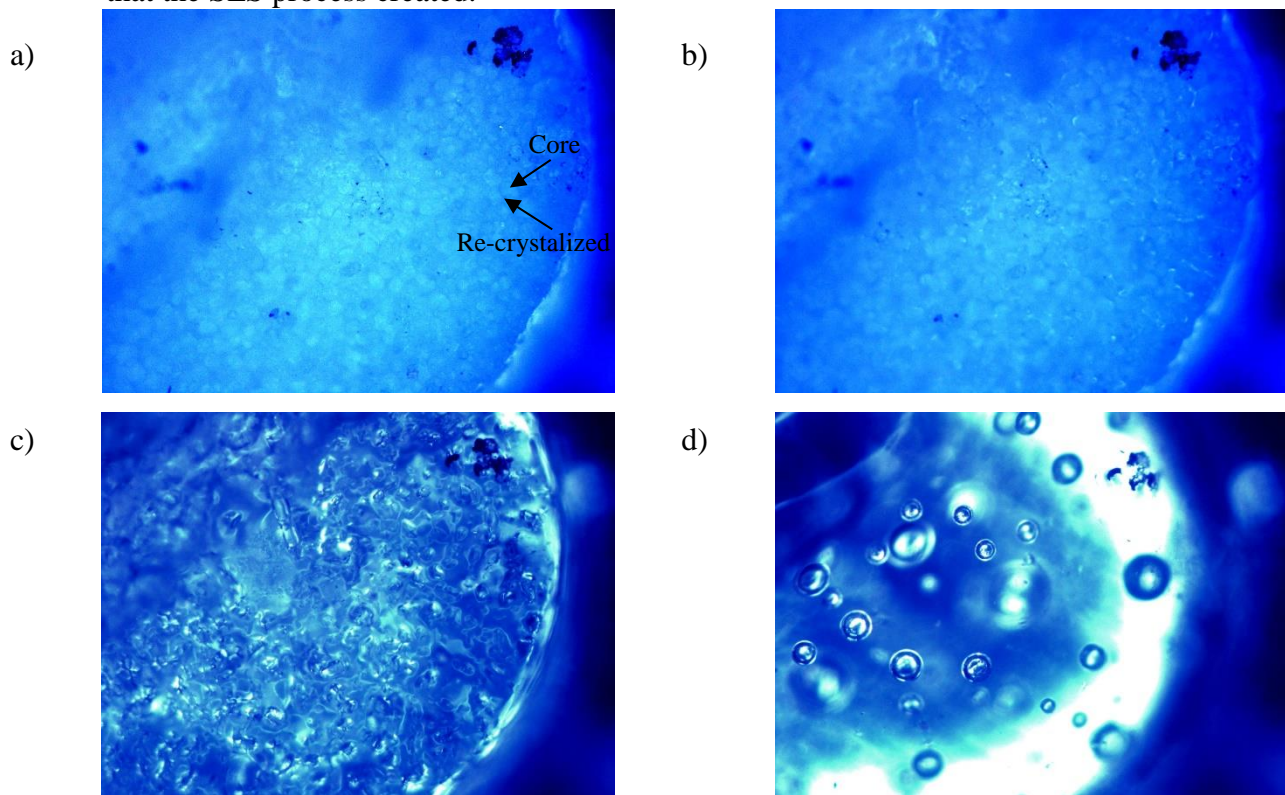


Figure 4.16 Microscopy images of sintered nylon 12 samples taken during DSC at approximately (a) 170 °C, (b) 178 °C, (c) 185 °C, and (d) 200 °C

To evaluate improvements in mechanical strength caused by the proposed laser control method, all flexure specimens were tested as described in section 4.2.2 and the results were separated into the two laser control techniques. Flexural strength results of all specimens of each control technique were run through an interquartile range (IQR) outlier detection algorithm that identified one specimen as having a strength outside 1.5 interquartile ranges. This component was disregarded to limit the influence of uncontrolled or random errors on the results. Of the remaining 99 specimens, 51 were built using a constant laser power while 48 were built using the ALC technique described. Figure 4.17(a) shows a histogram of flexural strengths for the fixed power and ALC specimens with a Gaussian distribution overlaid. The ALC components had a noticeably higher mean strength; however, this may be caused by the average post sintering temperature of the ALC bars being  $\sim 1.2$  °C hotter due to using a higher average laser power. This result, while real and measurable, was influenced by the choice of desired post-sintering temperature. If the desired post-sintering temperature was chosen to be the average post-sintering temperature of the fixed power control group, it is believed that the mean of both distributions would be equal. Figure 4.17(b) shows a more useful comparison where each distribution is normalized around its mean. As can be seen, using the automated laser control technique results in a 45% reduction in flexural strength standard deviation.

The ultimate flexural strength was also plotted against the average post-sintering temperature for each specimen in figure 4.18. The fixed power components, shown in red, exhibited a 5.4 °C temperature range and a large range in ultimate flexural strength that is correlated with post-sintering temperature. The ALC specimens, shown in blue, exhibited a temperature range of only 0.8 °C, despite the two techniques having

comparable pre-sintering temperature ranges (4.2 °C and 4.5 °C for the fixed power and ALC specimens, respectively).

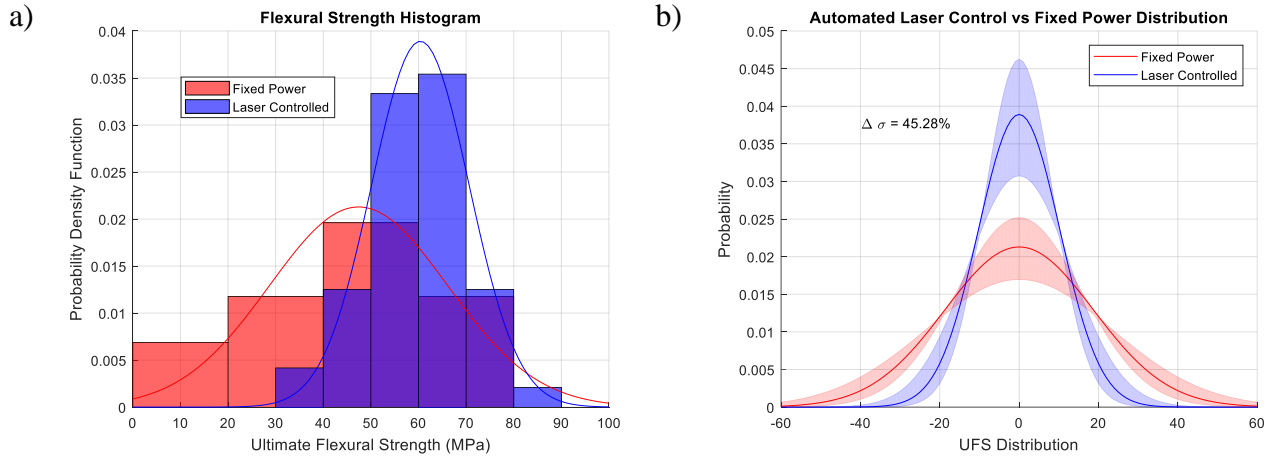


Figure 4.17: Flexural strengths of both control styles shown as (a) a histogram and (b) a Gaussian distribution plotted against their respective means

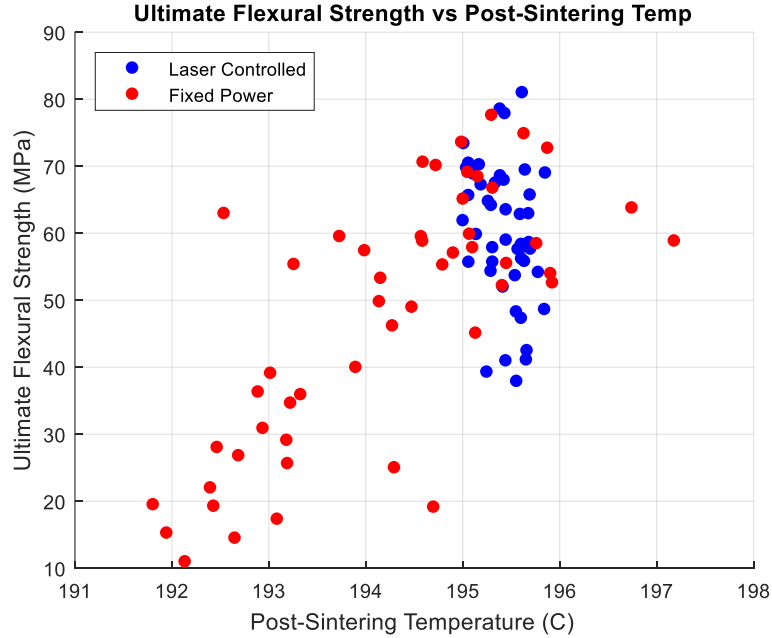


Figure 4.18 Ultimate flexural strength vs average post-sintering temperature

These results are extremely promising, as the reduced range of component strength is highly desired. The relatively large range produced in SLS and other additive manufacturing processes has been widely discussed as being one of the biggest issues with those processes. There are still some deficiencies in the controller proposed in this chapter, however. As this controller used a separate model for each component and did not allow laser power changes throughout the interior of a component, it is limited in application. For simple, constant cross-section components whose length dimensions are small compared with the length scale of the temperature gradients on the powder surface, this process works well. This is quite limiting, however, and disallows many of the properties and features that make AM useful. These deficiencies are addressed in Chapter 5 with the introduction of a new controller capable of real-time power modulation.

## **Chapter 5: Feed-Forward Active Laser Control**

This chapter will present the final form of the active laser controller developed. It will address the deficiencies of previous chapters by introducing a hardware solution allowing for real-time changes to laser power. It will also detail a more advanced power surface mapping that allows for continuous laser fluence adjustments over the entire build surface. Lastly, it will provide analysis of thermal results showing control over post-sintering temperatures for complex geometries.

### **5.1 POSITION-BASED LASER POWER CONTROLLER DESIGN**

At the time of writing, there are no commercial galvanometer controllers that allow laser power to be changed after the galvanometers have begun drawing a vector. This means that previous efforts to develop a laser power controller that relied on commercial hardware, including those introduced in chapters 3 and 4, functioned either by splitting vectors into subsections or by constraining power to be constant inside pre-defined areas. These techniques work well for small components or components that do not experience a large pre-sintering temperature gradient, but for larger components they are not capable of correcting for the temperature variations created by the powder pre-heat system. To develop a laser power controller suitable for complex and arbitrary geometries, it is crucial to enable intra-vector power modulation capabilities.

Some researchers have approached a similar laser power control problem by creating custom controllers [79] [47] that allow for laser power to be modulated independently of galvanometer movement. This approach, however, requires expensive hardware with low latency in order to properly synchronize the galvanometer movement with the laser pulse-width modulated (PWM) signal. It also presents a large programming task to replicate all the functionality offered by a commercial controller,

such as end of vector power ramping, standard XY2-100 galvanometer communication protocol, vector and contour definitions, accounting for galvanometer and laser latency, coordinate frame transformations, etc. It was decided a more appropriate approach for LAMPS was to develop a separate controller that works in conjunction with its Cambridge Technologies EC1000 laser controller. Much of the framework for this controller was done by Trevor Ricker and details of his implementation can be found in his thesis [80].

The solution developed by Ricker is termed the position-based laser power (PBLP) controller and is placed between the EC1000 and laser. The PBLP controller receives the laser power signal from the EC1000, real-time position feedback from the galvanometer controllers, and a mathematical representation of the desired power surface as inputs. The laser power signal is used as a trigger for the PBLP controller, which analyzes the signal to determine if the laser is supposed to be firing or not firing at any given moment. This allows the PBLP controller to have no knowledge of the scan path, yet still actuate the laser at the correct time intervals. The galvanometer position feedback is used in conjunction with the mathematical power surface to determine what the desired power is at the current laser position. When the laser power signal triggers the PBLP controller, it continuously samples the galvanometer position and generates the correct PWM signal according to the power surface.

The PBLP controller is housed on a National Instruments (NI) compactRio system with a Field-Programmable Gate Array (FPGA), a NI 9205 analog input module, and a NI 9402 digital input/output module. The NI 9205 module is used to measure the galvanometer position signal and has an update rate of  $4 \mu\text{s}$  ( $8 \mu\text{s}$  to collect both X and Y signals). The 9402 module is used to measure the laser power signal and generate the

PWM signal sent to the laser. This module has a maximum update rate of 55 ns. The laser scanning system complete with the PBLP controller can be seen in figure 5.1.

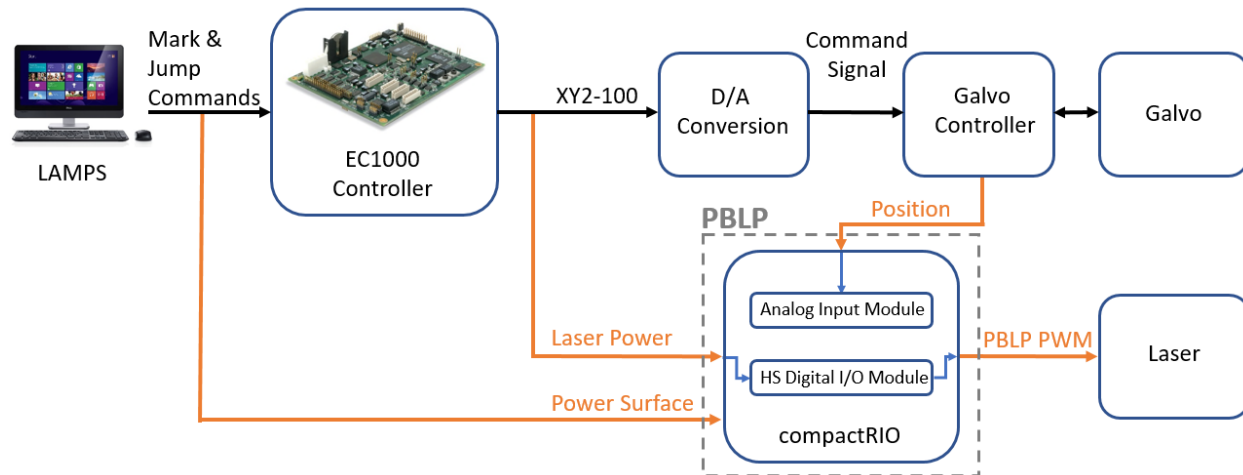


Figure 5.1 Position-Based Laser Power Controller

Ricker's implementation of the power surface was a 2-dimensional grid of laser power values that was bilinearly interpolated as the galvanometers drew [80]. This approach was imperfect in application due to the limited storage space on the FPGA that led to a coarse surface definition. To allow for a more complex surface without requiring more storage space, the PBLP controller was modified to allow for a 3rd order parametric power surface that describes desired laser power across the powder surface. FPGA solution of the parametric power surface is significantly faster than the standard laser duty cycle period of 100  $\mu$ s, meaning positional accuracy will not be lost due to latency in the PBLP controller. Further details on generating and implementing the power surface are given later on in this chapter.

## **5.2 CONTROLLER DESIGN**

The final automated laser control (ALC) implementation utilizes a feed-forward predictive model that calculates optimal laser powers across the powder bed, transforms those values into a parametric surface, then modulates the laser's power as it is drawn across the powder surface. In addition to the PBLP controller discussed in section 5.1, the ALC controller requires a more complex method of extracting thermal data from infrared images and using that data to build more accurate predictive models. These steps are detailed in the following sections.

### **5.2.1 Thermal Analysis**

Thermal data is recorded during the sintering process using a FLIR A6701 MWIR camera recording at 60 Hz. This process can generate more than 5 GB of data per layer, depending on the geometries being sintered. To reduce the size of data that needs to be analyzed, each layer's data is compressed into three images: the pre-sintering temperature, composite max post-sintering temperature, and the measured temperature increase. More information about the FLIR A6701 and how these images are formed can be found in section 4.1.

The ALC system is dependent on extracting thermal data from known location on the powder surface. To accomplish this, the thermal camera is first registered, creating a lookup table to transform from A6701 MWIR camera coordinate space to machine coordinate space. This is done by using the laser to create artifacts on the powder surface at known locations. These artifacts are detected in the thermal images and a least squares perspective transformation is applied to transform the thermal image. This process can be seen in figure 5.2. The lookup table created by the image registration process will take 640x512 pixels raw thermal images and transform them into 600x600 pixels registered

images. Next, a downsampling process reduces the resolution to 200x200 pixels by averaging each 3x3 pixels region on the registered image. Each pixel on this downsampled image corresponds to the average temperature of a 1mm x 1mm area on the powder surface. From this image, it is simple to query temperature at any location on the powder bed.

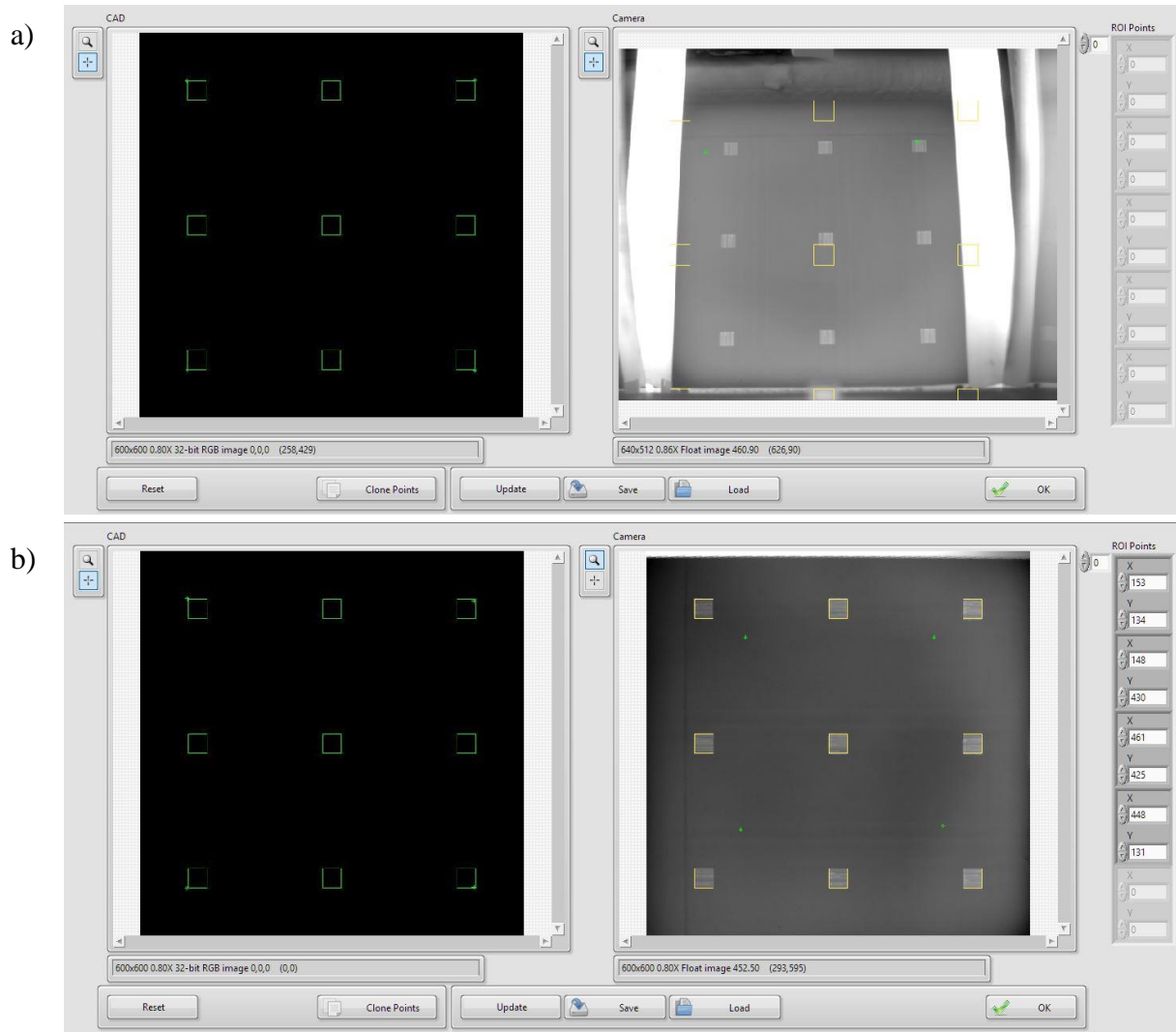


Figure 5.2 Thermal image registration process showing the laser sintered geometries on the left, (a) the raw thermal image, and (b) the registered image on the right with the laser sintered geometry overlaid

After the thermal images are registered, location-specific temperature values need to be extracted for the ALC system. The composite max post-sintering image has data extracted in order to build the thermal model and the pre-sintering image has data extracted to generate the laser power profiles. More information on these steps can be found sections 5.2.2 and 5.2.3. One method of extracting post-sintering thermal data is to use a threshold, above which it is believed that area on the powder surface experienced laser sintering. The difficulty with a simple threshold, though, is that often times the thermal data does not show a step change from not-sintered to sintered and instead shows a ramp up in post-sintering temperature. This makes choosing a reliable threshold value difficult. A more sophisticated method of determining which data to extract is to use that layer's laser scan file to determine exactly where sintering took place.

Generally, laser scan files for LAMPS are generated using General Electric's slicing software developed in conjunction with America Makes. The output from this slicing software is transformed into an XML document accepted by LAMPS' Cambridge Technology's EC1000 laser and galvanometer controller. The XML document can contain settings such as scan speed, laser power, delays, etc., but the majority of the document consists of MARK and JUMP commands that contain the laser scan vectors. To extract information pertaining to which areas of the powder bed were sintered, vertices of all components are extracted from the outline scans contained in the XML. Next, a blank image is created with the same dimensions as the downsampled MWIR data and each pixel is run through a point-in-polygon (PIP) test to determine if it is within one of the sintered objects defined in the XML. This creates a binary mask denoting sintering location. Some examples of XML scan files and their associated binary masks can be found in figure 5.3. These masks can then be applied to thermal images to isolate temperatures within the areas dictated by the laser scan file.



To extract thermal information, the composite max post-sintering image is run through the registration process described in section 5.2.1 to produce the downsampled image in machine coordinate space. Next, the binary sintering mask for the corresponding layer is applied to remove thermal data for any position not sintered. This step can be seen visually in figure 5.4. The pre-sintering temperature is subtracted from this image, resulting in temperature increase measurements at known locations for every area on the powder bed that underwent laser sintering. These thermal measurements are used in conjunction with laser power to build the thermal models.

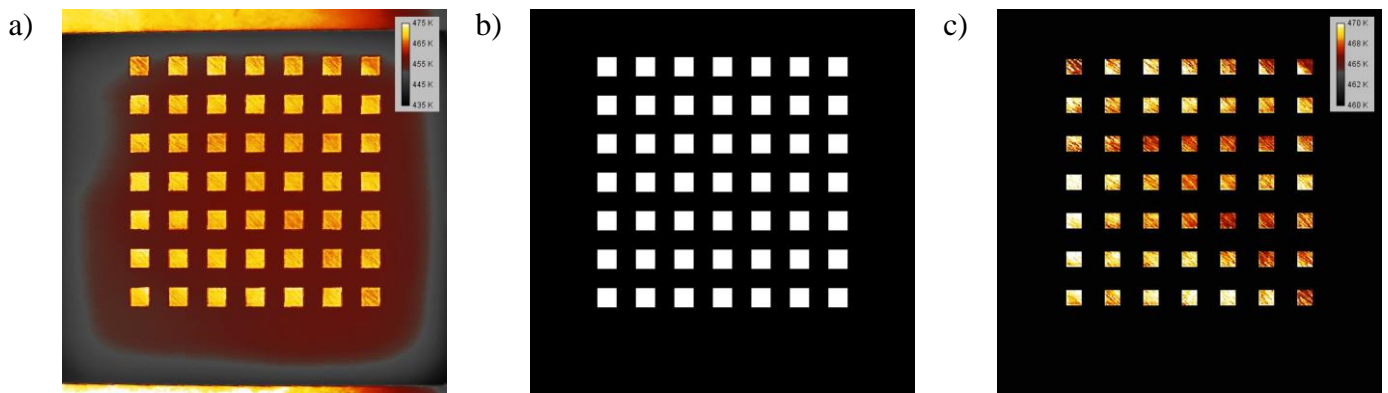


Figure 5.4 Images depicting (a) a composite max image after coordinate transformation into machine space, (b) the binary mask created from scan file, and (c) the composite max image with binary mask applied.

For each 1mm x 1mm area on the powder surface, weighted regression is used to create a model that relates laser power with expected temperature increase. Each model has the form of that in equation 5.1 and is initialized with the low boundary condition of 7% commanded laser power resulting in no temperature increase (this is the threshold for this particular laser and optic setup). Originally, an upper boundary condition for expected temperature rise at 100% laser power was also used to build the thermal model. This temperature rise value, however, was dependent on machine settings and maintenance schedule and can change from build to build, so hardcoding it as a boundary

condition resulted in suboptimal performance. This upper boundary condition was removed and replaced with using a fixed, predetermined laser power on the first layer of building. After the first layer, the thermal data extraction method described above was used and the temperature increase measurements were added to their respective model. At this point, each 1mm x 1mm area that experienced laser sintering has a thermal model consisting of the low boundary condition and the layer 1 thermal measurement. Both measurements receive full weighting and a linear regression is performed, though it is trivial at this point as the models only contains two values each.

$$P(T) = \beta_0 T + \beta_1 \quad \text{EQ 5.1}$$

**P** = Laser power (%)      **T** = Temperature rise      **β** = Fit coefficients

After subsequent layers, the newest post-sintering thermal measurement is added to the corresponding model with a full weight in the regression. Measurements from previous layers each have their weighting reduced, typically by 15%. An example of how the measurement weights change from layer 3 to layer 4 is given in figure 5.5. This introduces a forgetting factor that allows the models to deviate from old data so that the model can adapt to changes throughout the build process. This process of extracting data, recalculating regression weights, and fitting a linear model is repeated after every layer.

A visualization of a model for one 1mm x 1mm area after 10 layers can be seen in figure 5.6. Note that the laser power unit is percent of maximum output rather than watts. This was done because the energy impinging on the powder surface is not directly measurable during the build process. Additionally, the percent of laser energy lost through the optical track can change throughout a build due to contamination buildup on the optics [11] and can be non-uniform, causing a position-dependent loss [17]. Therefore, the commanded laser output is chosen as the system input and the model is

designed to account for the changes in laser power transmission. Data extraction and model building is accomplished during the recoat process between layers and adds an insignificant amount of time to the build. After this phase is complete and a new layer of powder has been spread, the ALC system enters the execute sintering phase described in section 5.2.3.

a)	<b>Layer</b>	-	1	2	3
	<b>Weight</b>	100	72	85	100
	<b>Power</b>	7	50	44	47
	<b>Temp (C)</b>	0	8.0	6.8	7.0
		$\beta_0 = 5.5$		$\beta_1 = 7.10$	

b)	<b>Layer</b>	-	1	2	3	4
	<b>Weight</b>	100	61	72	85	100
	<b>Power</b>	7	50	44	47	50
	<b>Temp (C)</b>	0	8.0	6.8	7.0	7.8
			$\beta_0 = 5.5$		$\beta_1 = 7.09$	

Figure 5.5 Example dataset after (a) 3 layers and (b) 4 layers showing the change in linear regression coefficients and how the weighting decreases due to the forgetting factor

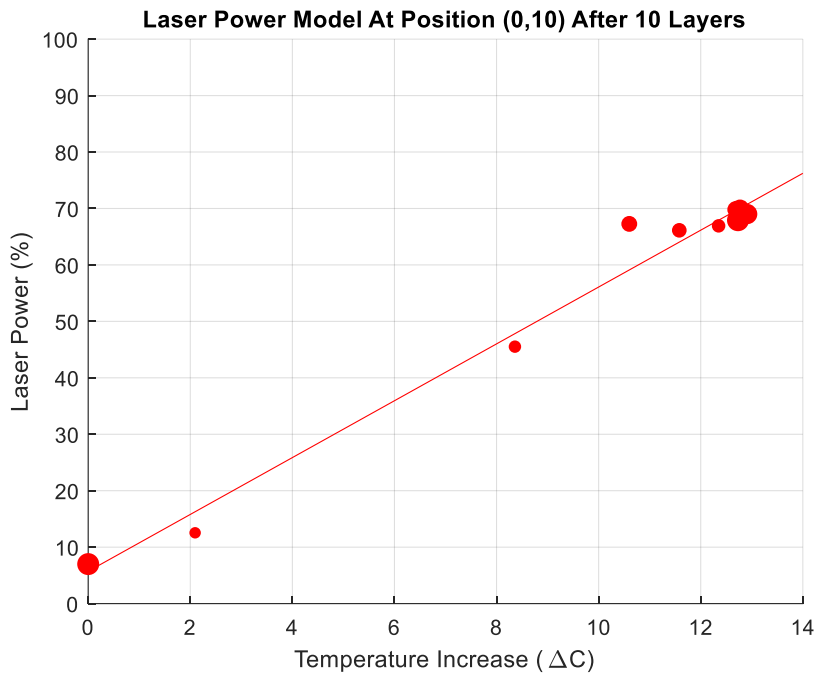


Figure 5.6 Example laser power model at position  $x = 0, y = 10$  after 10 layers of data

### 5.2.3 Execute Sintering

Once each new layer of powder is spread, the ALC system enters its execute sintering phase, where it will use pre-sintering thermal measurements and the empirical models to generate an optimal laser power surface that is actuated by the PBLP controller. This phase begins by using the A6701 MWIR camera to take a thermal image of the newly-spread powder surface. The pre-sintering temperature image is run through the registration and downsampling process described in section 5.2.1, the result of which can be seen in figure 5.7(a). These pre-sintering temperature values are compared with a desired post-sintering temperature to produce a desired temperature increase value for each 1mm x 1mm area on the powder surface, as seen in figure 5.7(b). Currently, the desired post-sintering value was found empirically through destructive testing of previously built parts; however, in the future it may be possible to develop a model that determines this value.

The desired temperature rise image has the binary sintering mask for the upcoming layer applied to remove data for powder areas that are not to be sintered, as seen in figure 5.7(c). This is done to improve surface fitting by allowing it to ignore data from insignificant locations. For every 1mm x 1mm area that the scan file indicates will be sintered, the thermal models created in section 5.2.2 are solved to calculate the optimal laser powers. These optimal powers and their locations are used to create a 3<sup>rd</sup> order surface via weighted regression. The form of the power surface is given in equation 5.2.

$$P(x, y) = \alpha_{00} + \alpha_{10}x + \alpha_{01}y + \alpha_{20}x^2 + \alpha_{11}xy + \alpha_{02}y^2 + \alpha_{30}x^3 + \alpha_{21}x^2y + \alpha_{12}xy^2 + \alpha_{03}y^3 \quad \text{EQ 5.2}$$

$P$  = Optimal laser power       $x, y$  = Location in machine coordinate space       $\alpha_{ij}$  = Surface coefficients

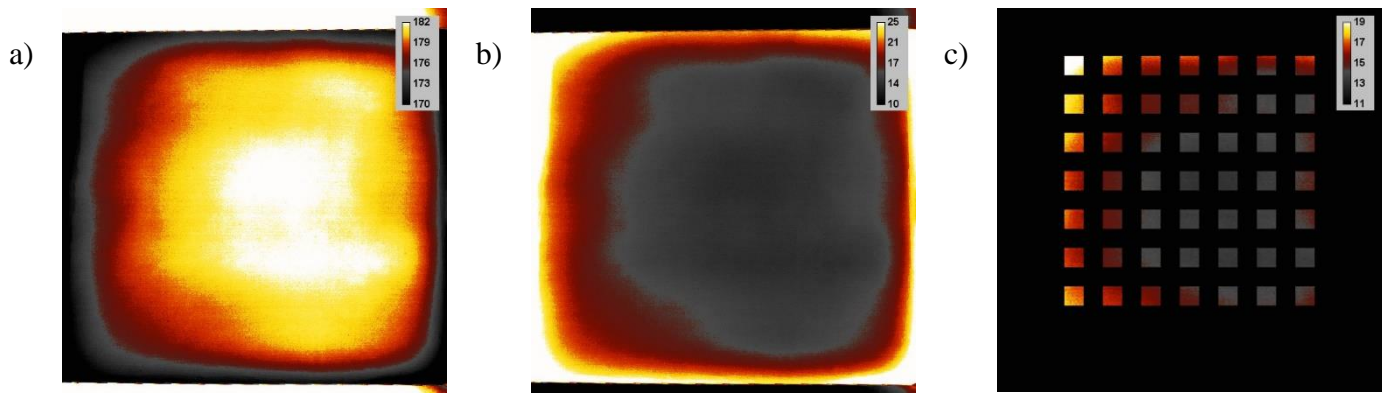


Figure 5.7 Thermal data showing (a) a registered pre-sintering image, (b) the desired temperature increase assuming a desired post-sintering temperature of 195 °C, and (c) the binary sintering mask for the upcoming layer applied to the desired temperature increase image.

The surface regression weighting factor for each 1mm x 1mm area comes from the number of layers that area has been previously sintered during the build. For example, imagine a simple rectangular component 10 mm in height with a step change in width after 8 mm that creates an unsupported overhang, as represented in figure 5.8(a). During the first 8 mm of the build, the ALC system collects 80 layers worth of data and the thermal model has a high level of accuracy for predicting optimal laser power in the sintered areas. The areas used in the thermal models to create the power surface for layer 80 are seen in figure 5.8(b). After layer 81, the system has sintered a new area it has not encountered before. The new thermal model areas are shown in figure 5.8(c), showing new geometry with only one layer's worth of data. The thermal models built in these new areas are expected to have larger errors in their laser power prediction abilities because they have less data to work with. Therefore, it is not desired to have these new thermal models dictate the power surface, though they should have some influence on it. On layer 82, then, the majority of the data used in the power surface regression should come from the original geometry that now has 81 layers worth of data, with only a minor influence by the new geometry that has a single layer of data. As the build continues,

more data is collected from this new area and the new models' predictive abilities improve so their relative weights are increased in the surface regression.

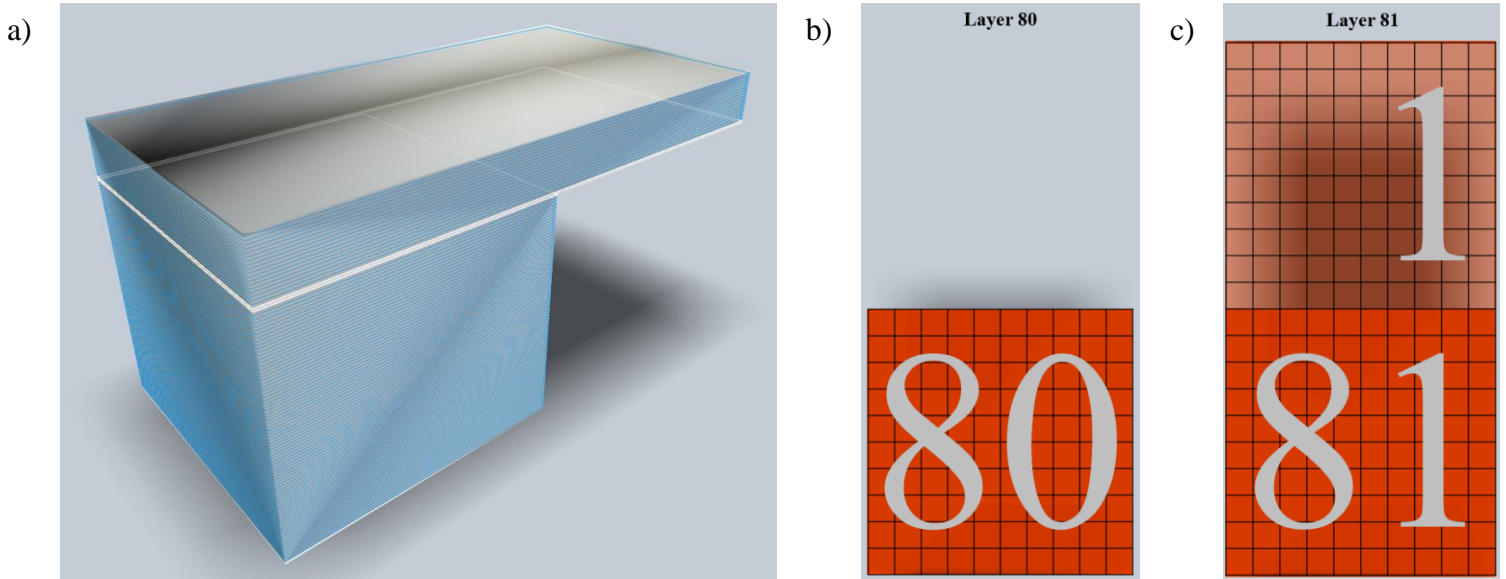


Figure 5.8 Example of power surface weighting for a component with non-constant geometry showing (a) a component with an unsupported overhang and a top down view of layers (b) 80 and (c) 81, where the step geometry change occurs. The orange grids show the 1mm x 1mm areas used in the thermal models with the number of data points for each grid overlaid.

An example power surface can be seen in figure 5.9, where the red data shows the calculated optimal power for each area to be sintered on this layer and the blue data shows the parametric power surface that will be sent to the PBLP controller. After the power surface is calculated, the laser begins sintering and the PBLP controller executes as described in section 5.1, using the coefficients to dictate the laser output. Once sintering is complete, the controller enters its build model phase, a new layer is spread, and the process is repeated.

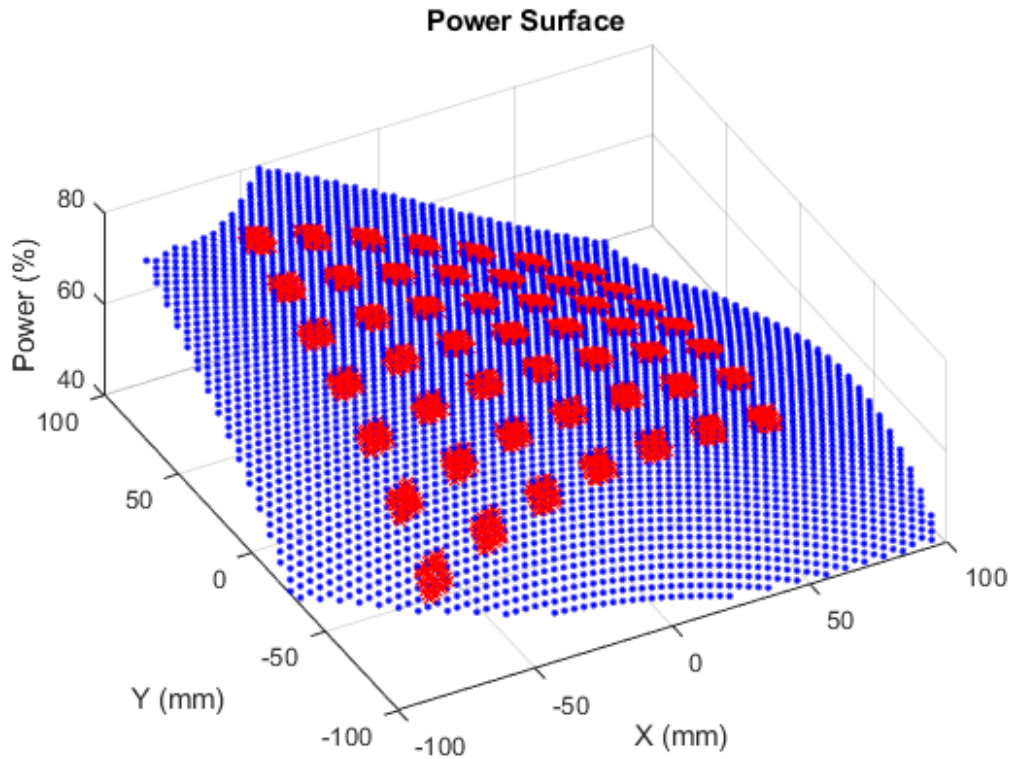


Figure 5.9 Example power surface sent to PBLP controller

### 5.3 CONTROLLER IMPLEMENTATION

The majority of LAMPS control is done through LabVIEW. All communication between the host computer and the motors, heaters, PBLP controller, galvanometer controller, and laser are done through LabVIEW. The ALC software, however, is written in C# and called through a dynamic link library (dll) in LabVIEW. All image manipulation, surface and linear regressions, and storage of the models is handled in C# due to its superior speed and flexibility.

Upon startup of the ALC system, LabVIEW creates an instance of the C# dll using a .NET constructor. The ALC software then creates a dictionary with 40,000 entries, one for each 1mm x 1mm area on the powder surface and populates each with the

thermal model initial conditions. The key for each dictionary entry is a unique x and y coordinate on the powder bed and the values for each key are arrays of layer number, pre-sintering temperature, laser power, measured temperature increase, and coefficients for the weighted linear regression at that position. This structure allows for probing the thermal model at any coordinate.

During the “build control model” phase of the ALC system, LabVIEW passes the ALC software the A6701 MWIR camera images collected on that layer and the location of the laser scan file that was just executed. The ALC software applies the image registration lookup table, downsamples the image, reads the laser scan file, and executes a PIP test to extract temperature information for every sintered area. For each area, the software solves the previous layer’s power surface at that coordinate and adds the calculated laser power to the dictionary entry along with the layer number, pre-sintering temperature, and temperature increase measurement. The layer number array is used to create an array of weights for the weighted linear regression that is applied to the arrays of laser power and temperature increase. The coefficients of the weighted regression are amended in the dictionary entry and will be used in future layers to predict optimal laser power.

During the “execute sintering” phase of the ALC system, LabVIEW passes the ALC software the pre-sintering thermal image and the location of the upcoming laser scan file. The ALC software again applies the image manipulations and laser scan file PIP test to extract pre-sintering thermal information. It then loops through every location to be sintered and uses the regression coefficients in the dictionary entry and the desired temperature increase to produce an optimal laser power value. After all laser powers are calculated, the ALC software uses a weighted surface regression algorithm to determine

an appropriate laser power surface. The coefficients of this surface are passed through LabVIEW to the PBLP controller on the FPGA.

### 5.4 EXPERIMENTS

The ALC system described in this chapter was evaluated by comparing thermal results produced using laser control with a baseline, fixed power test. All machine parameters were kept constant between the two builds, which consisted of 49 identical components each. The components were shaped like miniature I-beams with a 10mm x 10mm footprint with 10mm height. The full dimensions and arrangement can be seen in figure 5.10. High speed thermal image data was recorded with the A6701 MWIR camera throughout the entirety of the build process and was used to compare the two control techniques.

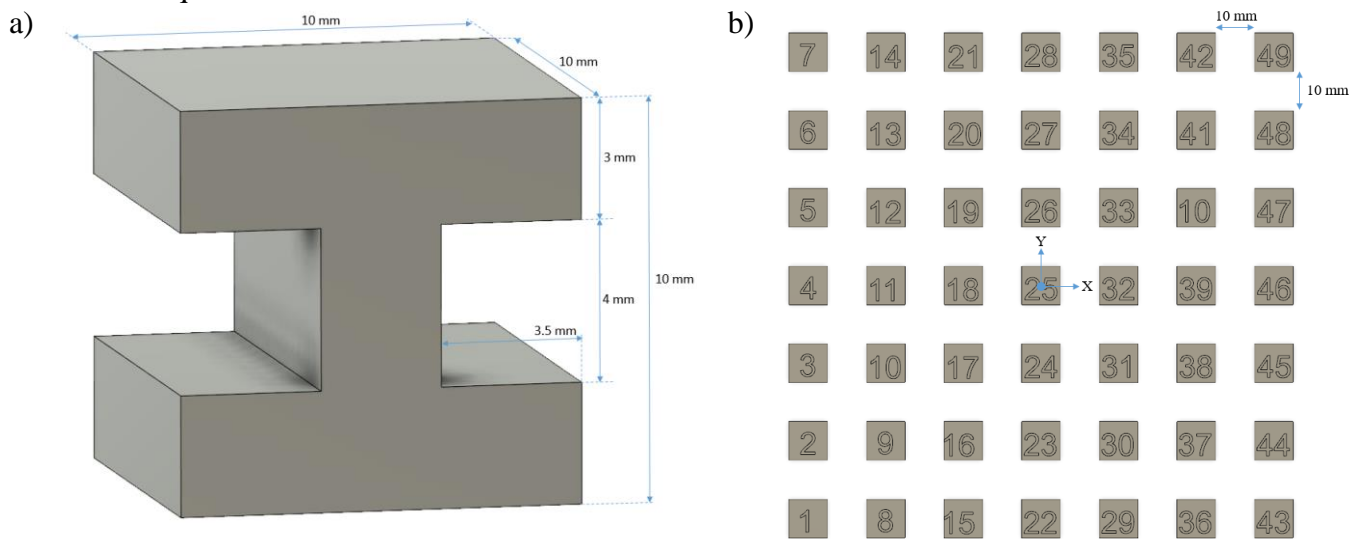


Figure 5.10 Dimensions of (a) test component and (b) their arrangement within the build chamber

## 5.5 RESULTS AND DISCUSSION

The tests described in section 5.4 were completed and the results of the baseline and Automated Laser Control builds were evaluated by comparing the composite max post-sintering temperatures, as described in section 4.1. The baseline test used a fixed laser power to replicate the control style implemented on most commercial SLS machines. Figure 5.11 tracks the average composite max post-sintering temperatures of 5 different components on each layer of the baseline build. The components displayed on this figure were located at the center and the four corners of the build chamber. As you can see, the range of temperatures on each layer for these components is approximately 9.5 °C and remains relatively constant as the build goes on. In contrast, figure 5.12 displays the same data for the ALC build and shows a significantly reduced temperature range. There is a large temperature variation during the first few layers, but as more data is collected and the model accuracy improves, the temperature range on each layer reduces to approximately 3.3 °C.

Thermal results from both builds show a sharp drop in post-sintering temperature at layer 70. This layer corresponds to when the cross-section goes from the 3mm x 10mm skinny section of the I-beam back to the 10mm x 10mm square section. While the ALC system did not completely anticipate and correct for the temperature drop caused by this step change in geometry, the temperature uniformity on this layer is still superior to that of the baseline test. The ALC results also show an unexplained dip in post-sintering temperature on layer 82 that caused the standard deviation of post-sintering temperatures to be worse than that of the baseline test, though the range was still improved. It is unclear what caused this temperature drop, but the ALC system self-corrected and quickly brought the post-sintering temperature standard deviation back within the desired range.

The improvements caused by Automated Laser Control on a layer-by-layer basis can be seen in figure 5.13, which shows the percent decrease in the range and standard deviations of post-sintering temperature on each layer when compared to the baseline test. Throughout the build, the laser control technique presented in this paper yielded improvements in temperature range and standard deviation of 52% and 33%, respectively, when comparing layer-to-layer temperatures. When comparing temperatures on a part-to-part basis, the improvement is even greater, at 65% and 47% for range and standard deviation.

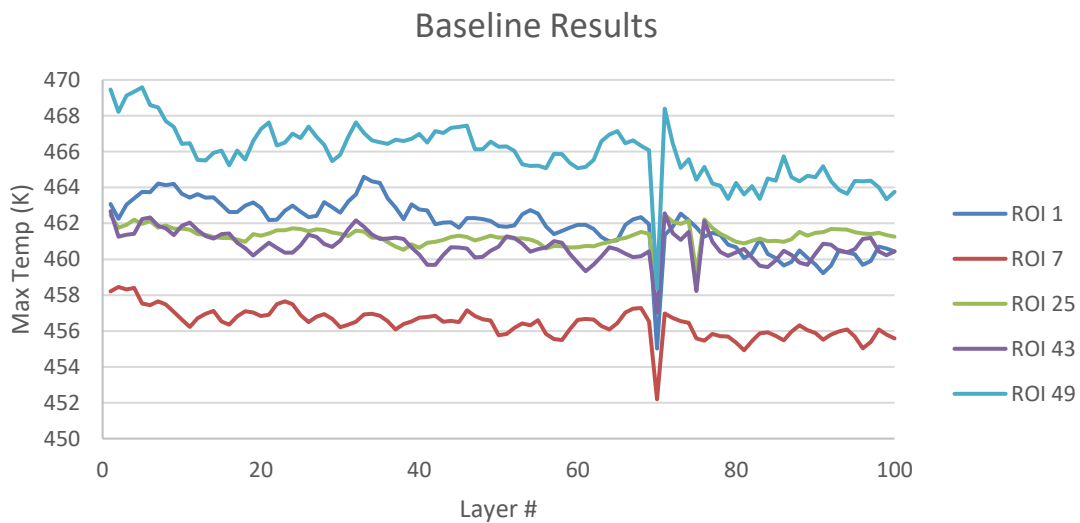


Figure 5.11 Results of baseline temperature testing of a complex geometry

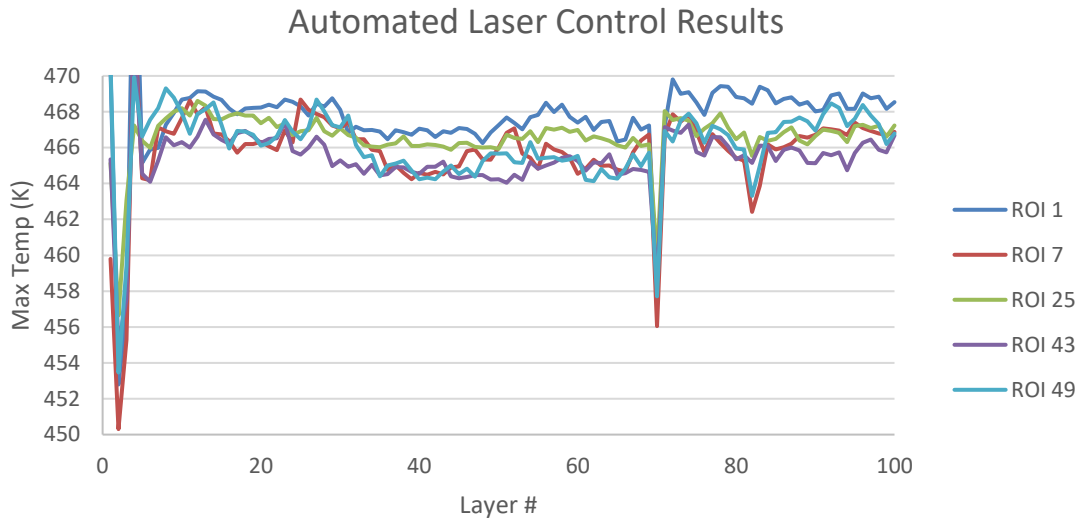


Figure 5.12 Results of Automated Laser Control temperature testing of a complex geometry

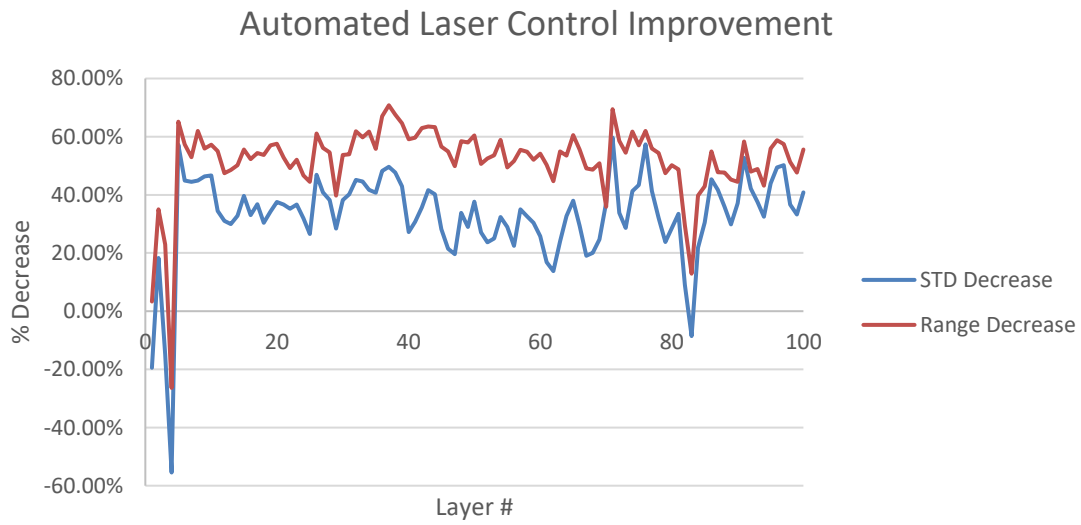


Figure 5.13 Improvement in temperature uniformity when using Automated Laser Control for a complex geometry

## Chapter 6: Conclusions

### 6.1 SUMMARY OF RESULTS

This dissertation presented a novel method for improving component consistency by developing an automated approach to controlling laser fluence based on thermal feedback. Due to limitations in sensor physics, real-time control methods were ruled out in favor of a feed-forward approach. A basic thermal model was reviewed and used for evaluating unique thermal conditions in the powder bed. The results of these simulations indicated that post-sintering temperature and melt depth can be controlled via laser fluence modulation. This finding was confirmed through thermal analysis in the LAMPS testbed, where preliminary testing was successful at reducing the influence of pre-existing temperature gradients on post-sintering temperatures. Multiple control methods were evaluated using thermal and mechanical tests. The ultimate control system, named Automated Laser Control (ALC), consisted of both hardware and software implementation that allows laser power to be controlled via a surface mapping that is created during runtime using dynamic surrogate modeling.

Thermal analysis was performed by using an infrared camera to capture post-sintering temperatures and evaluating component uniformity. Results from baseline testing that used a fixed laser power were compared with results from the ALC system. For simple geometries with a constant cross-section, the ALC system was able to reduce the standard deviation in post-sintering temperatures by approximately 57%. For complex geometries, the ALC system was able to reduce the standard deviation and range of post-sintering temperatures by 47% and 65%, respectively.

Mechanical strength of components was evaluated through destructive testing of standard flexure specimen. For these simple geometries, the ALC system resulted in a

45% reduction in standard deviation of ultimate flexural strength. Though no suitable testing standard exists for evaluating strength of the complex geometries built, it is believed that they would experience a comparable improvement in strength uniformity due to the similar improvements in thermal uniformity.

## **6.2 BROADER IMPACT**

The results presented here show promise at improving component uniformity in SLS, which has often been identified as one of its largest limiting factors [11] [53] [81]. The type of thermal analysis that is performed by the ALC software during runtime has also been shown to be useful for in-situ flaw detection [19] [63] and component qualification [53]. The combination of detection and correction provided by the ALC system create an incredibly powerful tool capable of decreasing costs and increasing utility, confidence, and industry adoption of SLS.

Testing on commercial SLS machines has revealed variations in mechanical properties of up to 25% under open-loop processing conditions [81] [82]. These variations lead to either a scrap rate that is significantly higher than traditional manufacturing processes or to a reduced material strength specification that can accommodate the variation without dropping below the reported value. Both of these situations are unfavorable as they increase cost and alter design guidelines. Reducing this variability, then, is highly desired and can be accomplished via the proposed ALC system.

Approximately 90-95% of commercial SLS components are made from a polyamide-based material due, in part, to its comparatively simple processing [8] [9]. This lack of additional engineering materials has been identified as another limitation of SLS with significant research focused on developing new materials [83]. The difficulty

with many of these new AM materials, such as PPS, PEEK, and PEK, are that they are more challenging to build with due to their higher sensitivity to build conditions. Improving thermal control in SLS with ALC, thus, opens the door to new materials research and can potentially increase SLS use cases.

### **6.3 FUTURE WORK**

Several areas of future work have been identified that could potentially broaden the impact of the work presented in this dissertation. Firstly, throughout testing of the ALC system, empirical values were used for determining optimal post-sintering temperatures. One avenue of future work would be to replace this empirical value with one found via physics modeling. It is possible that the optimal post-sintering temperature is not constant in all cases. For example, in cases of sintering of virgin powder or unsupported overhangs it is possible that the differences in conduction paths would necessitate a different post-sintering temperature to ensure similar melt depths. The ALC system that was developed is capable of targeting non-constant post-sintering temperatures and would be able to accommodate such a task if modeling or further testing found evidence that it would improve component quality. Additionally, identifying the maximum pixel value on each layer as the post-sintering temperature may ignore some potentially useful information. Looking at the time history of pixel temperatures during the build may reveal supplementary information that can improve temperature measurement.

A second avenue of exploration that may improve the accuracy of the ALC controller is to develop a pre-build protocol for initializing the thermal models. Using the ALC system to collect data prior to building of critical components may reduce or eliminate the wild post-sintering temperature fluctuations observed during the first few

layers of sintering. One common technique used in industrial SLS is building multiple small, thin pieces at the start of every build, termed a heat shield, in hopes of decreasing temperature gradients on subsequent layers. It may be possible to incorporate model initialization with the heat shield building process to improve model accuracy during critical components without extending the build time.

Testing of the final ALC system, presented in chapter 5, focused on evaluating post-sintering temperature uniformity. While this is an important result and can be used to infer an improvement in mechanical properties, component strength was not explicitly tested in complex geometries. To further improve confidence in the ALC system, a third avenue of further work would be to apply additional tests to ALC-built components to directly measure physical and mechanical properties. Properties such as tensile and flexure strength, density, crystallinity, and elongation at break could be measured and used to compare with baseline SLS components.

All of the testing presented in this dissertation was accomplished using ALM PA650 Nylon 12 material. While nylon makes up the majority of SLS material, it would be prudent to test the ALC system on other materials. Many of the other SLS materials are more difficult to build with and could potentially see an even greater benefit than nylon. Additionally, the improved control made achievable by the ALC system may aid in development and testing of other novel SLS materials. Applying ALC to these other SLS materials would likely further increase its utility.

The ALC system presented shows great promise at improving SLS component quality, but one of the big barriers to bringing this technology to market is cost. The biggest material cost of the system is the mid-wave infrared camera. Identification of alternative, less expensive sensors or other cost-saving alterations could lead to more widespread adoption of this system. Even with the limitations identified, the controller

presented in this dissertation has proven to be capable of significantly improving component consistency in SLS and can be utilized in both research and commercial applications to improve outcomes.

## Appendices

### APPENDIX A: LIST OF TERMS AND ABBREVIATIONS

$\alpha_{ij}$	Power surface coefficients
$b$	Flexure bar width
$\beta$	Extinction coefficient
$\beta_i$	Linear regression coefficients
$c$	Speed of light
$c_p$	Specific heat capacity
$C_2$	Planck's second radiation constant, $hc/k$
$d$	Flexure bar depth
$\epsilon$	Emissivity
$h$	Planck's constant
$h_t$	Heat transfer coefficient
$H$	Enthalpy
$k$	Boltzmann's constant
$k_t$	Thermal conductivity
$L_f$	Latent heat of fusion
$L$	Flexure test support span
$\lambda$	Wavelength
$M$	Spectral emittance
$m$	Mass
$P$	Flexure test load
$Q$	Laser source radiation
$R$	Reflectivity
$\rho$	Density
$\sigma$	Stefan-Boltzmann constant
$\sigma_f$	Flexural strength
$T$	Temperature
$t$	Simulation time
$\tau$	Optical transmission
$v$	Laser beam velocity
$W$	Radiant power
$w$	Radius of Gaussian beam
$x,y,z$	Machine coordinates

<b>2D</b>	Two-dimensional
<b>3D</b>	Three-dimensional
<b>ALC</b>	Automated Laser Control
<b>ALM</b>	Advanced Laser Materials
<b>AM</b>	Additive Manufacturing
<b>CAD</b>	Computer-Aided Design
<b>CCD</b>	Charge-Coupled Device
<b>CMOS</b>	Complementary Metal–Oxide–Semiconductor
<b>DLL</b>	Dynamic-Link Library
<b>DPM</b>	Degree of Particle Melt
<b>DSC</b>	Differential Scanning Calorimetry
<b>EOS</b>	Electro-Optical Systems, GmbH
<b>FPGA</b>	Field-Programmable Gate Array
<b>IQR</b>	Interquartile Range
<b>IR</b>	Infrared
<b>LAMPS</b>	Laser Additive Manufacturing Pilot System
<b>LWIR</b>	Long-Wave Infrared
<b>MWIR</b>	Mid-Wave Infrared
<b>NI</b>	National Instruments
<b>OCT</b>	Optical Coherence Tomography
<b>PA</b>	Polyamide
<b>PBF</b>	Powder Bed Fusion
<b>PBLP</b>	Position-Based Laser Power
<b>PEEK</b>	Polyether Ether Ketone
<b>PEK</b>	Polyetherketone
<b>PID</b>	Proportional, Integral, Derivative
<b>PIP</b>	Point-In-Polygon
<b>PPS</b>	Polyphenylene Sulfide
<b>PWM</b>	Pulse-Width Modulated
<b>SLM</b>	Selective Laser Melting
<b>SLS</b>	Selective Laser Sintering
<b>STD</b>	Standard Deviation
<b>SWIR</b>	Short-Wave Infrared
<b>ZnSe</b>	Zinc Selenide

## APPENDIX B: SELECTED CODE

### Perspective Transformation

```
public float[,] TransformMatrix(int[] Xp, int[] Yp, int[] Xr, int[] Yr)
{
    float[,] gamma = this.gamma(Xp, Yp, Xr, Yr);
    float[] beta = this.beta(Xr, Yr);
    float[,] partialTransVec = m_matrixMath.Multiply(gamma, beta);
    float[,] transMat = new float[3, 3];
    transMat[0, 0] = partialTransVec[0, 0];
    transMat[0, 1] = partialTransVec[1, 0];
    transMat[0, 2] = partialTransVec[2, 0];
    transMat[1, 0] = partialTransVec[3, 0];
    transMat[1, 1] = partialTransVec[4, 0];
    transMat[1, 2] = partialTransVec[5, 0];
    transMat[2, 0] = partialTransVec[6, 0];
    transMat[2, 1] = partialTransVec[7, 0];
    transMat[2, 2] = 1;
    return transMat;
}

public float[,] gamma(int[] Xp, int[] Yp, int[] Xr, int[] Yr)
{
    float[,] alpha = this.alpha(Xp, Yp, Xr, Yr);
    return m_matrixMath.Multiply(m_matrixMath.Invert(m_matrixMath.Multiply(m_matrixMath.Transpose(alpha), alpha)), m_matrixMath.Transpose(alpha));
}

public float[,] alpha(int[] Xp, int[] Yp, int[] Xr, int[] Yr)
{
    float[,] subAlpha = new float[2 * Xp.Length][]; //pre-allocate alpha
    for (int i = 0; i < Xp.Length; i++)
    {
        subAlpha[2 * i] = new float[] { Xp[i], Yp[i], 1, 0, 0, 0, -Xr[i] * Xp[i], -Xr[i] * Yp[i] };
        subAlpha[2 * i + 1] = new float[] { 0, 0, 0, Xp[i], Yp[i], 1, -Yr[i] * Xp[i], -Yr[i] * Yp[i] };
    }
    return m_matrixMath.Convert(subAlpha);
}

public float[] beta(int[] Xr, int[] Yr)
{
    int nXr = Xr.Length;
    int nYr = Yr.Length;
    float[] beta = new float[nXr + nYr];
    for (int i = 0; i < nXr; i++)
    {
        beta[2 * i] = Xr[i];
        beta[2 * i + 1] = Yr[i];
    }
    return beta;
}

public int[,] CreateLUT(float[,] TransformMatrix, int heightOut, int widthOut)
{
    int[,] LUT = new int[widthOut + 1, 2 * heightOut];
    LUT[0, 0] = heightOut;
    LUT[0, 1] = widthOut;
    Parallel.For(0, widthOut, i =>
    {
        for (int j = 0; j < heightOut; j++)
        {
            float[] pos = { i, j, 1 };

            float[,] coeff = m_matrixMath.Multiply(TransformMatrix, pos);
            int Xp = (int)Math.Round(coeff[1, 0] / coeff[2, 0]);
            int Yp = (int)Math.Round(coeff[0, 0] / coeff[2, 0]);
            LUT[i + 1, 2 * j] = Xp;
            LUT[i + 1, 2 * j + 1] = Yp;
        }
    });
    return LUT;
}
```

## Add Thermal Measurements to Model

```
public void dictAddLayerData(float[,] ImgMaskedIR, double[] alpha, int layer)
{
    for (int y = 0; y < 200; y++)
    {
        for (int x = 0; x < 200; x++)
        {
            if (ImgMaskedIR[y, x] > 0)
            {
                int xMM = -100 + x;
                int yMM = 99 - y;
                double pow = this.solveSurfaceRegression(xMM, yMM, alpha);
                this.dictAppend(layer, xMM, yMM, pow, (double)ImgMaskedIR[y, x], 0.85);
            }
        }
    }
}

public void dictAppend(int layer, int Xmm, int Ymm, double power, double temp, double extinctionCoeff)
{
    string evenOdd = "Odd";
    if (layer % 2 == 0)
    {
        evenOdd = "Even";
    }
    if (AltLayers == false)
    {
        evenOdd = "Even";
    }
    LayerProperties layerProp;
    layerProp.Xmm = Xmm;
    layerProp.Ymm = Ymm;
    layerProp.LayerAlt = evenOdd;

    LayerValues vals = LayerDictionary[layerProp];
    List<double> pows = vals.power.ToList<double>();
    List<double> temps = vals.temp.ToList<double>();
    List<int> layers = vals.Layer.ToList<int>();
    pows.Add(power);
    temps.Add(temp);
    layers.Add(layer);

    double[] weights = new double[pows.Count];
    weights[0] = 100;
    if (pows.Count > 1)
    {
        for (int i = 1; i < pows.Count; i++)
        {
            weights[i] = 100 * Math.Pow(extinctionCoeff, (layer - layers[i]));
        }
    }
    vals.power = pows.ToArray();
    vals.temp = temps.ToArray();
    vals.Layer = layers.ToArray();
    vals.coeff = MathNet.Numerics.Fit.PolynomialWeighted(vals.temp, vals.power, weights, 1);
    LayerDictionary[layerProp] = vals;
}
```

## Power Surface Regression

```
public double[] SurfaceRegression(float[,] tempIncrease)
{
    //Assemble X input
    double[][] X = new double[LayerDictionary.Count][];
    double[] P = new double[LayerDictionary.Count];
    double[] W = new double[LayerDictionary.Count];
    List<double[]> lstX = new List<double[]>(); //X and Y inputs
    List<double> lstP = new List<double>(); //Power
    List<double> lstW = new List<double>(); //Weights
    //For Each
    #region
    foreach (KeyValuePair<LayerProperties, LayerValues> entry in LayerDictionary)
    {
        double xTemp = centerAndScale(entry.Key.Xmm);
        double yTemp = centerAndScale(entry.Key.Ymm);
        int xInd = entry.Key.Xmm + 100;
        int yInd = 99 - entry.Key.Ymm;
        double[] tempX = new double[10];
        tempX[0] = 1;
        tempX[1] = xTemp;
        tempX[2] = yTemp;
        tempX[3] = xTemp * xTemp;
        tempX[4] = xTemp * yTemp;
        tempX[5] = yTemp * yTemp;
        tempX[6] = Math.Pow(xTemp, 3);
        tempX[7] = Math.Pow(xTemp, 2) * yTemp;
        tempX[8] = Math.Pow(yTemp, 2) * xTemp;
        tempX[9] = Math.Pow(yTemp, 3);
        lstX.Add(tempX); //X and Y inputs
        lstP.Add(MathNet.Numerics.Evaluate.Polynomial(tempIncrease[yInd, xInd], entry.Value.coeff)); //Calculate Optimal Laser Power
        if (tempIncrease[yInd, xInd] == 0)
        {
            lstW.Add(0);
        }
        else
        {
            lstW.Add(5 * (entry.Value.power.Count() - 1));
        }
        X = lstX.ToArray(); //X and Y inputs
        P = lstP.ToArray(); //Calculate Optimal Laser Power
        W = lstW.ToArray(); ;
    }
    #endregion

    double weight = W.Sum();
    double[] alpha = new double[10];
    P = P.Select(v => v > 100 ? 100 : v).ToArray();
    if (weight > 0)
    {
        alpha = MathNet.Numerics.LinearRegression.WeightedRegression.Weighted(X, P, W);
    }
    else
    {
        alpha = MathNet.Numerics.LinearRegression.MultipleRegression.DirectMethod(X, P);
    }
    this.setCoefficients(alpha);
    return alpha;
}
```

## Apply Binary Mask

```
public float[,] applySinterMask(float[,] img, double[] x, double[] y, string XMLpath, int shrink)
{
    //Run point in polygon test to generate verteces of each object
    bool[] mask = new bool[x.Length];
    double[,] polygons = clsLayerRead.complexPartBoundary(XMLpath);
    int numPoly = polygons.GetLength(0);
    for (int ind = 0; ind < x.Length; ind++)
    {
        double[] xy = new double[2] { x[ind], y[ind] };
        for (int poly = 0; poly < numPoly; poly++)
        {
            mask[ind] = clsLayerRead.pointInPolygon(xy, polygons[poly], mask[ind]);
        }
    }
    //Erode mask
    int imgWidth = img.GetLength(1);
    int width = 1 + (2 * shrink);
    int half_width = (width - 1) / 2;
    int[] Kernel = new int[width * width];
    float[] imgVect = ConvertToVector(img);
    float[] maskedVect = new float[imgVect.Length];
    float[] maskedVectShrink = new float[imgVect.Length];
    for (int i = 0; i < imgVect.Length; i++)
    {
        bool edge = false;
        int indKernel = 0;
        maskedVect[i] = mask[i] ? imgVect[i] : 0;
        for (int r = -width / 2; r <= width / 2; r++)
        {
            for (int c = -width / 2; c <= width / 2; c++)
            {
                Kernel[indKernel] = i + r * imgWidth + c;
                indKernel++;
                edge = edge || (i + r * imgWidth + c < 0);
            }
        }
        if (!edge)
        {
            bool maskSame = true;
            for (int j = 0; j < Kernel.Length; j++)
            {
                maskSame = maskSame && mask[Kernel[j]];
                if (!maskSame)
                    break;
            }
            maskedVectShrink[i] = !maskSame ? 0 : maskedVect[i];
        }
    }
    return ConvertToImage(maskedVectShrink, img.GetLength(0), img.GetLength(1));
}
```

## Point In Polygon Test

```
public static bool pointInPolygon(double[] testPoint, double[,] polygon, bool inPolygon)
{
    int numVert = polygon.GetLength(1);
    for (int i = 0, j = numVert-1; i < numVert; j = i++)
    {
        if ( ((polygon[1, i] > testPoint[1]) != (polygon[1, j] > testPoint[1])) &&
            (testPoint[0] < (polygon[0, j] - polygon[0, i]) * (testPoint[1] - polygon[1, i]) / (polygon[1, j] - polygon[1, i]) + polygon[0, i]) )
            inPolygon = !inPolygon;
    }
    return inPolygon;
}
```

## Works Cited

- [1] A. Lindstrom, "Selective Laser Sintering, Birth of an Industry," 6 December 2012. [Online]. Available: <http://www.me.utexas.edu/news/news/selective-laser-sintering-birth-of-an-industry>.
- [2] A. S. 52900, "Standard Terminology for Additive Manufacturing - General Principles - Terminology," 2015.
- [3] K. R. Bakshi and A. V. Mulay, "A Review on Selective Laser Sintering: A Rapid Prototyping Technology," *IOSR Journal of Mechanical & Civil Engineering*, vol. 4, pp. 53-57, 2016.
- [4] L. Columbus, "The State of 3D Printing, 2017," *Forbes*, 23 May 2017. [Online].
- [5] S. Fish, J. C. Booth, S. T. Kubiak, W. W. Wroe, A. D. Bryant, D. R. Moser and J. J. Beaman, "Design and subsystem development of a high temperature selective laser sintering machine for enhanced process monitoring and control," *Addit Manuf*, vol. 15, pp. 60-67, 2015.
- [6] A. Lewis, N. Katta, A. McElroy, T. Milner, S. Fish and J. Beaman, "Understanding and improving optical coherence tomography imaging depth in selective laser sintering nylon 12 parts and powder," *Optical Engineering*, vol. 57, no. 4, 2018.
- [7] M. Gardner, A. Lewis, J. Park, A. McElroy, A. Estrada, S. Fish, J. Beaman and T. Milner, "In situ process monitoring in selective laser sintering using optical coherence tomography," *Optical Engineering*, vol. 57, no. 4, 2018.
- [8] J. P. Kruth, G. Levy, R. Schindel, T. Craeghs and E. Yasa, "Consolidation of Polymer Powders by Selective Laser Sintering," in *Proceedings of the 3rd International Conference on Polymers and Moulds Innovations*, 2008.
- [9] T. Wohlers, "Wohlers Report 2014: 3D Printing and Additive Manufacturing State of the Industry Annual Worldwide Progress Report," Wohlers Associates, 2014.
- [10] Advanced Laser Materials, "PA650 Technical Data Sheet," Temple, 2011.
- [11] D. L. Bourell, T. J. Watt, D. K. Leigh and B. Fulcher, "Performance limitations in polymer laser sintering," *Physics Procedia*, vol. 56, pp. 147-156, 2014.
- [12] M. Zhao, K. Wudy and D. Drummer, "Crystallization Kinetics of Polyamide 12 during Selective Laser Sintering," *Polymers*, vol. 10, no. 2, 2018.
- [13] H. Budzier and G. Gerlach, *Thermal Infrared Sensors: Theory, Optimisation and Practice*, Hoboken: Wiley, 2010.
- [14] W. Minkina and S. Dudzik, *Infrared Thermography Errors and Uncertainties*, John Wiley & Sons, 2009.
- [15] J. P. Kruth, X. Wang, T. Laoui and L. Froyen, "Lasers and materials in selective laser sintering," *Assembly Automation*, vol. 23, no. 4, pp. 357-371, 2003.
- [16] T. Diller, R. Sreenivasan, J. Beaman, D. Bourell and J. LaRocco, "Thermal Model of the Build Environment for Polyamide Powder Selective Laser Sintering," in *Solid Freeform Fabrication Symposium*, Austin, 2010.
- [17] D. Sassaman, P. Hall, S. Fish and J. Beaman, "Two-dimensional Characterization of Window Contamination in Selective Laser Sintering," in *Solid Freeform Fabrication Symposium*, Austin,

- 2018.
- [18] B. Caulfield, P. E. McHugh and S. Lohfeld, "Dependence of mechanical properties of polyamide components on build parameters in the SLS process," *J of Mater Process Technol*, vol. 182, pp. 477-488, 2007.
- [19] W. W. Wroe, J. Gladstone, T. Phillips, S. Fish, J. Beaman and A. McElroy, "In-situ thermal image correlation with mechanical properties of nylon-12 in SLS," *Rapid Prototyping Journal*, vol. 22, no. 5, pp. 794-800, 2016.
- [20] S. Negi, S. Dhiman and R. K. Sharma, "Determining the effect of sintering conditions on mechanical properties of laser sintered glass filled polyamide parts using RSM," *Materials*, vol. 68, pp. 205-218, 2015.
- [21] I. Gibson and S. Dongping, "Material properties and fabrication parameters in selective laser sintering process," *Rapid Prototyping Journal*, vol. 3, no. 4, pp. 129-136, 1997.
- [22] S. Singh, V. S. Sharma, A. Sachdeva and S. K. Sinha, "Optimization and analysis of mechanical properties for selective laser sintered polyamide parts," *Materials & Manufacturing Processes*, vol. 28, pp. 163-172, 2013.
- [23] T. Phillips, S. Fish and J. Beaman, "Development of an automated laser control system for improving temperature uniformity and controlling component strength in selective laser sintering," *Additive Manufacturing*, vol. 24, pp. 316-322, 2018.
- [24] J. A. Benda, "Temperature-Controlled Selective Laser Sintering," in *Solid Freeform Fabrication Symposium*, Austin, 1994.
- [25] H. Ho, I. Gibson and W. Cheung, "Effects of energy density on morphology and properties of selective laser sintered polycarbonate," *Journal of Materials Processing Technology*, pp. 89-90, 1999.
- [26] S. T. Kubiak, "Characterization of Quartz Lamps Emitters for High Temperature Polymer Selective Laser Sintering (SLS) Applications," MS Thesis, University of Texas at Austin, 2013.
- [27] T. Craeghs, S. Clijsters, E. Yasa and J.-P. Kruth, "Online Quality Control of Selective Laser Melting," in *Solid Freeform Fabrication Symposium*, Austin, 2011.
- [28] T. G. Spears and G. A. Scott, "In-process sensing in selective laser melting (SLM) additive manufacturing," *Integrating Materials and Manufacturing Innovation*, 2016.
- [29] A. Tapetado, J. Diaz-Alvarez, M. H. Miguelez and C. Vasquez, "Tw-Color Pyrometer for Process Temperature Measurement During Machining," *Journal of Lightwave Technology*, vol. 34, 2016.
- [30] M. Ignatiev, I. Smurov and G. Flamant, "Real-time optical pyrometry in laser machining," *Measurement Science and Technology*, vol. 5, 1994.
- [31] I. Smurov and M. Doubenskaia, "Optical sensing in laser machining," *Optical Sensors*, 2009.
- [32] B. Muller and U. Renz, "Development of a fast fiber-optic two-color pyrometer for the temperature measurement of surfaces with varying emissivities," *Review of Scientific Instruments*, vol. 72, pp. 3366-3374, 2001.
- [33] J. Thevenet, M. Siroux and B. Desmet, "Measurements of brake disk surface temperature and emissivity by two-color pyrometry," *Applied Thermal Engineering*, vol. 30, pp. 753-759, 2010.

- [34] F. J. Madruga, A. G. Fernandez and J. M. Lopez-Higuera, "Error Estimation in a Fiber-Optic Dual Waveband Ratio Pyrometer," *IEEE Sensors Journal*, vol. 4, 2004.
- [35] W. Corporation. [Online]. Available: [www.WilliamsonIR.com](http://www.WilliamsonIR.com).
- [36] Y. Chivel and I. Smurov, "On-line temperature monitoring in selective laser sintering/melting," *Physics Procedia*, vol. 5, 2010.
- [37] M. Doubenskaia, M. Pavlov and Y. Chivel, "Optical system for on-line monitoring and temperature control in selective laser melting technology," *Key Engineering Materials*, vol. 437, 2010.
- [38] M. Speka, S. Mattei, P. Michel and M. Ilie, "The infrared thermography control of the laser welding of amorphous polymers," *NDT&E International*, vol. 41, 2008.
- [39] T. Phillips, A. McElroy, S. Fish and J. Beaman, "In-Situ Laser Control Method for Polymer Selective Laser Sintering (SLS)," in *Proceedings of the 26th Annual International Solid Freeform Fabrication Symposium – An Additive Manufacturing Conference*, Austin, 2016.
- [40] T. Fu, J. Zhao, M. Zhong and C. Shi, "Two-color optical charge-coupled-device-based pyrometer using two-peak filter," *Review of Scientific Instruments*, vol. 81, 2010.
- [41] G. Zauner, D. Heim, K. Niel, G. Hendorfer and H. Stoeri, "CCD Cameras as Thermal Imaging Devices in Heat Treatment Processes," *Machine Vision Applications in Industrial Inspection*, vol. 12, 2004.
- [42] F. Bardin, S. Morgan, S. Williams, R. McBride, A. J. Moore, J. D. C. Jones and D. P. Hand, "Process control of laser conduction welding by thermal imaging measurement with a color camera," *Applied Optics*, vol. 44, no. 32, 2005.
- [43] S. Clijsters, T. Craeghs, S. Buls, K. Kempen and J. P. Kruth, "In Situ quality control of the selective laser melting process using a high-speed, real-time melt pool monitoring system," *Int J Adv Manuf Technol*, vol. 75, 2014.
- [44] S. Kaierle, "Process Monitoring and Control of Laser Beam Welding".
- [45] H. Chmelickova, H. Sebestova, M. Havelkova, L. Rihakova and L. Nozka, "Laser welding control by monitoring of plasma," *Optical Measurement Systems for Industrial Inspection*, vol. 8, 2013.
- [46] C. Bagger and F. O. Olsen, "Laser welding closed-loop power control," *Journal of Laser Applications*, vol. 15, no. 1, 2003.
- [47] B. Fulcher, *Real-time Pyrometer Feedback and Control in Metal Powder Bed Fusion*, Austin: paper presented to Solid Freeform Fabrication Symposium, 2018.
- [48] EOS, "EOS P 396 - About 38% less energy consumption and up to 32% faster," [Online]. Available: [https://www.eos.info/systems\\_solutions/plastic/systems\\_equipment/eos\\_p\\_396](https://www.eos.info/systems_solutions/plastic/systems_equipment/eos_p_396). [Accessed February 2019].
- [49] S. Paternoster, F. Muller and A. Fruth, "Method and Device for the Improved Control of the Energy Input in a Generative Layer Construction Method". United States of America Patent US2016332379 (A1), 17 November 2016.
- [50] P. Keller, Interviewee, *Head of Material and Process Development at EOS*. [Interview]. 8 September 2017.

- [51] C. Baur, Interviewee, *Manager - R&D and Applications Development - Polymers at EOS*. [Interview]. 4 December 2018.
- [52] M. Abdelrahman and T. L. Starr, "Feedforward Control for Polymer Laser Sintering Process Using Part Geometry," in *Solid Freeform Fabrication Symposium*, Austin, 2015.
- [53] M. Abdelrahman and T. L. Starr, "Quality certification and control of polymer laser sintering: layerwise temperature monitoring using thermal imaging," *International Journal of Advanced Manufacturing Technology*, vol. 84, pp. 831-842, 2016.
- [54] C. Nelson, S. Xue, J. Barlow, J. Beaman, H. Marcus and D. Bourell, "Model of the selective laser sintering of bisphenol-A polycarbonate," *Industrial & Engineering Chemistry Research*, vol. 32, no. 10, pp. 2305-2317, 1993.
- [55] W. W. Duley, *Laser Processing and Analysis of Materials*, New York: Springer US, 1983.
- [56] M.-s. Sun and J. Beaman, "A Three Dimensional Model for Selective Laser Sintering," in *2nd Annual International Solid Freeform Fabrication Symposium - An Additive Manufacturing Conference*, Austin, 1991.
- [57] J. F. Ready, "Properties of lasers," in *Effects of high-power laser radiation*, New York, Academic Press, 1971.
- [58] D. Moser, S. Fish, J. Beaman and J. Murthy, "Multi-Layer Computational Modeling of Selective Laser Sintering Processes," in *ASME International Mechanical Engineering Congress and Exposition*, Montreal, 2014.
- [59] D. Moser, "Multi-Scale Computational Modeling of Selective Laser Melting for Process Improvements," Austin, 2017.
- [60] L. Dong, A. Makradi, S. Ahzi and Y. Remond, "Three-dimensional transient finite element analysis of the selective laser sintering process," *Journal of Materials Processing Technology*, vol. 209, no. 2, pp. 700-706, 2009.
- [61] I. A. Roberts, C. J. Wang, R. Esterlein, M. Stanford and D. Mynors, "A three-dimensional finite element analysis of the temperature field during laser melting of metal powders in additive layer manufacturing," *International Journal of Machine Tools and Manufacture*, vol. 49, no. 12, pp. 916-923, 2009.
- [62] T. W. Becker and B. J. P. Kaus, "Numerical Modeling of Earch Systems," University of Southern California, Los Angeles, 2016.
- [63] T. Phillips, L. Zhang, S. Fish and J. Beaman, "Laser Power Control in SLS," in *Solid Freeform Fabrication Symposium*, Austin, 2017.
- [64] J. R. Rajan and K. L. Wood, "Experimental Study of Selective Laser Sintering of Parmax," The University of Texas at Austin, 2001.
- [65] A. Gopal and B. Ravani, "Physical Modeling for Selective Laser Sintering," *J of Comput and Inf Sci in Eng*, vol. 17, no. 2, 2017.
- [66] C. Schick, "Differential scanning calorimetry (DSC) of semicrystalline polymers," *Analytical and Bioanalytical Chemistry*, pp. 1589-1611, 2009.
- [67] Y. Kong and J. N. Hay, "The enthalpy of fusion and degree of crystallinity of polymers as

- measured by DSC," *European Polymer Journal*, vol. 39, pp. 1721-1727, 2009.
- [68] Mettler Toledo, "DSC Analysis - Fundamentals and Applications," [Online]. Available: [https://www.mt.com/hk/en/home/library/on-demand-webinars/lab-analytical-instruments/DSC\\_TA.html](https://www.mt.com/hk/en/home/library/on-demand-webinars/lab-analytical-instruments/DSC_TA.html). [Accessed 14 February 2019].
- [69] J. M. Ward and J. Sweeney, *Mechanical Properties of Solid Polymers*, third edition, Chichester: John Wiley & Sons, 2013.
- [70] W. J. Sichina, "DSC as Problem Solving Tool: Measurement of Percent Crystallinity of Thermoplastics," 2000. [Online]. Available: [http://www.perkinelmer.com/Content/applicationnotes/app\\_thermalcrystallinitythermoplastics.pdf](http://www.perkinelmer.com/Content/applicationnotes/app_thermalcrystallinitythermoplastics.pdf). [Accessed 14 February 2019].
- [71] H. Zarringhalam, C. Majewski and N. Hopkinson, "Degree of particle melt in Nylon-12 selective laser-sintered parts," *Rapid Prototyping Journal*, vol. 15, no. 2, pp. 126-132, 2009.
- [72] N. Hopkinson, C. E. Majewski and H. Zarringhalam, "Quantifying the degree of particle melt in Selective Laser Sintering," *CIRP Annals - Manufacturing Technology*, vol. 58, pp. 197-200, 2009.
- [73] Y. Li, X. Zhu, G. Tian, D. Yan and E. Zhou, "Multiple melting endotherms in melt-crystallized nylon 10, 12," *Polymer International*, vol. 50, pp. 677-682, 2001.
- [74] C.-L. Wei, M. Chen and F.-E. Yu, "Temperature modulated DSC and DSC studies on the origin of double melting peaks in poly(ether ether ketone)," *Polymer*, vol. 44, pp. 8185-8193, 2003.
- [75] Y. Wang, C. M. DiNapoli, G. A. Tofig, R. W. Cunningham and R. A. Pearson, "Selective Laser Sintering Processing Behavior of Polyamide Powders," in *SPE ANTEC*, Anaheim, 2017.
- [76] "ASTM D3417 Standard Test Method for Enthalpies of Fusion and Crystallization of Polymers by Differential Scanning Calorimetry (DSC)," ASTM International, West Conshohocken, PA, 1999.
- [77] "ASTM D790-17 Standard Test Methods for Flexural Properties of Unreinforced and Reinforced Plastics and Electrical Insulating Materials," ASTM International, West Conshohocken, PA, 2017.
- [78] C. C. Chamis, "Analysis of the three-point-bend test for materials with unequal tension and compression properties," *Natl. Aeronaut and Space Adm*, Cleveland, 1974.
- [79] B. Lane, S. Mekhontsev, S. Grantham, M. L. Vlasea, J. Whiting, H. Yeung, J. Fox, C. Zarobila, J. Neira, M. McGlaflin, L. Hanssen, S. Moylan, A. Donmez and J. Rice, "Design, developments, and results from the NIST additive manufacturing metrology testbed (AMMT)," in *Solid Freeform Fabrication Symposium*, Austin, 2016.
- [80] T. Ricker, "Position Based Laser Power (PBLP) Control for Selective Laser Sintering (SLS)," University of Texas at Austin Master's Thesis, Austin, 2017.
- [81] W. Cooke, R. A. Tomlinson, R. Burguete, D. Johns and G. Vanard, "Anisotropy, homogeneity and ageing in an SLS polymer," *Rapid Prototyping Journal*, vol. 17, no. 4, pp. 269-279, 2011.
- [82] M. Faes, Y. Wang, P. Lava and D. Moens, "Variability in the mechanical properties of laser sintered PA-12 components," in *Solid Freeform Fabrication Symposium*, Austin, 2015.
- [83] R. D. Goodridge, C. J. Tuck and R. J. M. Hague, "Laser sintering of polyamides and other polymers," *Progress in Materials Science*, vol. 57, pp. 229-267, 2012.